Helsinki University of Technology Laboratory of Biomedical Engineering
Department of Engineering Physics and Mathematics
Teknillinen korkeakoulu Lääketieteellisen tekniikan laboratorio Teknillisen fysiikan ja matematiikan osasto
Espoo 2002

CONTEXTUAL DETECTION OF FMRI ACTIVATIONS AND MULTIMODAL ASPECTS OF BRAIN IMAGING

Eero Salli

TEKNILLINEN KORKEAKOULU
TEKNISKA HÖGSKOLAN
HELSINKI UNIVERSITY OF TECHNOLOGY
TECHNISCHE UNIVERSITÄT HELSINKI
UNIVERSITE DE TECHNOLOGIE D´HELSINKI

Helsinki University of Technology Laboratory of Biomedical Engineering
Department of Engineering Physics and Mathematics
Teknillinen korkeakoulu Lääketieteellisen tekniikan laboratorio
Teknillisen fysiikan ja matematiikan osasto
Espoo 2002

CONTEXTUAL DETECTION OF FMRI ACTIVATIONS AND MULTIMODAL ASPECTS OF BRAIN IMAGING

Eero Salli

Dissertation for the degree of Doctor of Science in Technology to be presented with due permission of the Department of Engineering Physics and Mathematics for public examination and debate in Auditorium F1 at Helsinki University of Technology (Espoo, Finland) on the 8th of August, 2002, at 12 noon.

ISBN (printed) 951-22-6029-8
ISBN (pdf) 951-22-6030-1

Picaset Oy
Helsinki 2002

Abstract

Functional magnetic resonance imaging (fMRI) is a non-invasive method which can be used to indirectly localize neuronal activations in the human brain. Functional MRI is based on changes in the blood oxygenation level near the activated tissue. In an fMRI experiment, a stimulus is given to a subject or the subject is asked to conduct a physical or cognitive task. During the experiment, a nuclear magnetic resonance signal is measured outside the head, and time series of three-dimensional image volumes are constructed. The object of this thesis is to study the localization of activation regions from the constructed time series as well as multimodal aspects of brain imaging. The localization of activation regions typically consists of the following phases: preprocessing of the four-dimensional spatiotemporal data, computation of a statistic image, and detection of statistically significantly activated regions from the statistic image. The statistic image is a three-dimensional map, which shows the statistical significance of the measured experimental effect at voxel level. The detection and localization of the activated regions can be carried out by segmenting the statistic image into activated and non-activated regions. The segmentation is difficult because the statistic images are often noisy and high specificity requirements are set for the activation localization. In this thesis, a computationally efficient segmentation method has been developed. The method is based on the utilization of contextual information from the 3-D neighborhood of each voxel by using a Markov random field model. The method does not require assumptions about the intensity distribution of the activated voxels. The method has been tested using both simulated and measured fMRI data. The use of contextual information increased the detection rate of weakly activated regions. In the simulation experiments, spatial autocorrelations in the noise term altered overall false-positive rates only little. It was also demonstrated that the developed method preserved spatial resolution better than the commonly used linear spatial filtering. In repeated fMRI experiments, variation in the activated regions obtained by the developed method was about the same as or less than with other widely used methods. In addition to the activation localization, the use of multimodal data, including the comparison of fMRI and magnetoencephalographic (MEG) data, is discussed in this thesis. This thesis also includes multimodal visualization examples created from MEG, single photon emission computed tomography, fMRI and structural magnetic resonance imaging data.

Keywords: fMRI, activation localization, segmentation, contextual information, multimodality, visualization

Preface

The work for this thesis was carried out in the image processing group of the Laboratory of Biomedical Engineering, Helsinki University of Technology, and in the functional brain imaging unit of the Department of Radiology, Helsinki University Central Hospital (HUCH). Both the image processing group and the functional brain imaging unit are member units of the Helsinki Brain Research Centre (HBRC).

I wish to thank Professor Toivo Katila, the supervisor of this thesis, for all discussions and for providing excellent research environment for this work. I would also like to thank my instructors Professor Hannu Aronen and Professor Ari Visa for the research ideas and valuable guidance.

I am grateful to all co-workers at HUCH, especially Antti Korvenoja, M.D., for planning and carrying out many of the imaging sessions of this work. The discussions I had with him during the course of this thesis have been inspiring and motivating. I also sincerely thank Hanna Pohjonen, D.Sc. (Tech.), Docent Sauli Savolainen, Docent Risto Ilmoniemi, Docent Synnöve Carlson and Mr. Sami Martinkauppi for their many contributions to this work.

I would like to thank the preliminary examiners, Professor Risto Kauppinen and Dr. Stephen Smith for their corrections and suggestions for improving this thesis. Many thanks are also due to Kaarina Poutiainen, M.A., for correcting the language of the manuscript.

In addition, the people at the Laboratory of Biomedical Engineering, especially the former and current members of the image processing group, deserve my thanks for assistance and providing an inspiring atmosphere.

The financial support provided by the Foundation of Technology in Finland, the Radiological Society of Finland, the Jenny and Antti Wihuri Foundation, and the Research Foundation of Helsinki University of Technology is gratefully acknowledged.

Finally, I want to express my gratitude to my parents, my brother and my sister for their support. Last, but certainly not least, I thank my wife Päivi for her support, patience and encouragement during this work.

Espoo, May 2002

Eero Salli

Contents

List of publications

This thesis consists of an overview and of the following six publications:

I E. Salli, H. J. Aronen, S. Savolainen, A. Korvenoja and A. Visa (2001). Contextual clustering for analysis of functional MRI data. *IEEE Trans. Med. Imaging* 20:403–414.

II E. Salli, A. Visa, H. J. Aronen, A. Korvenoja and T. Katila (1999). Statistical segmentation of fMRI activations using contextual clustering. In *Proc. of the 2nd International conference on Medical Image Computing and Computer Assisted Intervention (MICCAI'99)*. C. Taylor, A. Colchester (Eds.). Springer. *Lect. Notes Comput. Sci.* 1679:481–488.

III E. Salli, A. Korvenoja, A. Visa, T. Katila and H. J. Aronen (2001). Reproducibility of fMRI: Effect of the use of contextual information. *NeuroImage* 13:459–471.

IV A. Korvenoja, J. Huttunen, E. Salli, H. Pohjonen, S. Martinkauppi, J. M. Palva, L. Lauronen, J. Virtanen, R. J. Ilmoniemi and H. J. Aronen (1999). Activation of multiple cortical areas in response to somatosensory stimulation: Combined magnetoencephalographic and functional magnetic resonance imaging. *Hum. Brain Mapp.* 8:13–27.

V H. Pohjonen, O. Sipilä, V.-P. Poutanen, S. Bondestam, K. Somer, E. Salli, A. Korvenoja, P. Nikkinen, H. J. Aronen, R. J. Ilmoniemi, T. Katila, K. Liewendahl and C.-G. Standertskjöld-Nordenstam (1996). Hospital-wide PACS: multimodal image analysis using ATM network. In *Computer Assisted Radiology: Proc. of the International Symposium on Computer and Communication Systems for Image Guided Diagnosis and Therapy (CAR'96)*. H. U. Lemke, M. W. Vannier, K. Inamura, A. G. Farman (Eds.). Elsevier. Pages 399–404.

VI H. Pohjonen, P. Nikkinen, O. Sipilä, J. Launes, E. Salli, O. Salonen, P. Karp, J. Ylä-Jääski, T. Katila and K. Liewendahl (1996). Registration and display of brain SPECT and MRI using external markers. *Neuroradiology* 38:108–114.

List of abbreviations and symbols

BOLD	blood oxygenation level-dependent
CNR	contrast-to-noise ratio
CSF	cerebral spinal fluid
ECD	equivalent current dipole
EPI	echo-planar imaging
FIR	finite impulse response
fMRI	functional magnetic resonance imaging
FPQ	fundamental power quotient
FPR	false-positive rate
FWHM	full width at half maximum
GLM	general linear model
GM	gray matter
HRF	hemodynamic response function
ICM	iterated conditional modes
KS	Kolmogorov-Smirnov
MAP	maximum a posteriori
MEG	magnetoencephalography
ML	maximum likelihood
MMP	maximum marginal probability
MR	magnetic resonance
MRF	Markov random field
MRI	magnetic resonance imaging
$N(\mu, \sigma^2)$	Normal distribution with mean μ and variance σ^2
NIR	Near-infrared
PET	positron emission tomography
RF	radio frequency
ROC	receiver operator characteristic
SA	simulated annealing
SI	statistic image
SMA	supplementary motor area
SMI	primary sensorimotor cortex
SNR	signal-to-noise ratio
SPE(C)T	single photon emission (computed) tomography
SPM	statistical parametric mapping
SVD	singular value decomposition
WM	white matter
n-D	n-dimensional

1 Introduction

Our understanding of the human brain and its function at macroscopic, microscopic and molecular levels has greatly increased during the last decades. Remarkable advances have been made in molecular and cellular level research and in gene technology including the identification of genes responsible for various diseases and results of single-neuron recordings (Kandel and Squire, 2000). The development of functional brain imaging methods producing time series of volumetric data, like positron emission tomography (PET) and functional magnetic resonance imaging (fMRI), has provided an ability to monitor neural activity in the whole brain area. The functional imaging methods produce huge amount of data, which has created a need for efficient data analysis, processing and visualization methods.

Magnetic resonance imaging (MRI) is nowadays the ultimate method in obtaining images of human brain structure non-invasively. At the beginning of the 90s it was noted that the principles of MRI can also be used to image the function of the brain (Ogawa et al., 1990, 1992; Belliveau et al., 1991; Kwong et al., 1992). In most fMRI experiments, blood serves as an endogenous contrast agent to image hemodynamics accompanying neuronal activation. It is said that fMRI has revolutionized cognitive neuroscience and neurofunctional imaging (Menon, 2001; Lai et al., 2000). Functional MRI, together with other brain mapping methods like PET, electroencephalography (EEG) and magnetoencephalography (MEG), has increased knowledge of the human brain function. For example, new information has been obtained about motor function, perception, face recognition, learning and memory (Rosen et al., 1998; Rowe and Frackowiak, 1999; Moonen and Bandettini, 2000). As a non-invasive method fMRI can also be used on children and the studies can be repeated several times on a same subject. This allows the monitoring of changes in cortical organization during learning and development. Potential clinical applications of fMRI include pre-surgical localization of functionally important brain areas, detection of functional abnormalities in developmental disorders, monitoring of brain damage and recovery of function, monitoring of effectiveness of therapeutic interventions (e.g. drugs and different rehabilitation strategies) and investigation of cerebral correlates of mental illness (Moonen and Bandettini, 2000; Turner and Ordidge, 2000).

While fMRI measures the relatively slow hemodynamic changes associated with neural activity, EEG and MEG measure the electric or magnetic fields generated by neuronal activity. The temporal and spatial characteristics of the methods complement each other. Single photon emission computed tomography (SPECT) provides information about physiological function and can be used to diagnose various abnormalities like cerebral infarcts, brain tumors, inflammatory diseases and epilepsy, among many other applications. Anatomical localization of the abnormalities is sometimes difficult but can be improved by adding structural information from MR images. These examples illustrate that different imaging modalities provide complementary information, and fusing the data from different imaging modalities is often beneficial. Some related multimodal aspects, like comparison of different modalities and visualization, are presented in this work.

A frequent goal of fMRI data analysis is to recognize activated brain areas, i.e. image regions whose intensity changes are induced by the stimulus given to a subject. The analysis of fMRI data is complicated for several reasons. Task- or stimulus-induced signal-change-to-signal-noise ratio (contrast-to-noise ratio, CNR) is often low. Noise sources include thermal

noise, physiological fluctuations, effects caused by movements of the subject and instrumental instabilities. In many cases (e.g. with visual stimulus), the voxels[1] of the strongest "activations" may show signal changes of tens of percents, especially when small voxels are used to reduce partial volume effects [e.g. Oja et al. (1999a)]. However, the histogram of activation-related signal changes may be broad and include small changes. Large signal changes often arise from relatively large venous vessels (Kim et al., 2000) rather than from the smaller venules and capillaries closer to the activated neuronal tissue. Typical magnitudes of signal changes in tasks involving primary sensory or primary motor areas are of the order of a few percent, and in cognitive tasks of the order of one percent or so. To detect these subtle changes from the noise, the measurements are usually repeated several times over a long period of time, which, in turn, may lead to problems associated with subject motion and scanner instabilities. The second complication of fMRI data analysis is the large size of datasets, typically tens of megabytes in size. Analysis of these data sets requires a great deal of storage space, powerful computers and efficient data analysis methods. In addition, autocorrelated noise makes it more difficult to draw statistical inferences.

In this work, the localization of the activated regions has been studied as a segmentation problem: how to divide an image into activated and non-activated areas. The term "segmentation" implicitly includes not only the detection and localization, but also the delineation of the activated regions. Usually a 3-D statistic image (SI), also called a statistical map, is computed from the four-dimensional spatiotemporal fMRI data after preprocessing steps. The effects of signal variations originating from physiology or scanner instabilities are minimized by means of study design and data preprocessing and during the computation of the SI. The intensities of non-activated voxels of the SI are assumed to follow a known distribution, e.g. the standard normal distribution $N(0,1)$, and activated voxels unknown distributions. The segmentation of the SI represents a special type of segmentation problem in which the distribution of the background (null distribution) voxels is known but the distributions of the object (activated regions) voxels are not. A traditional approach is to threshold the computed SI. Together the computation of the SI and its thresholding consist of a large number of hypothesis tests, one for each voxel. A voxel is considered to be activated if the test rejects a null hypothesis that the voxel is not activated. It is important to note that in addition to the task-induced signal change, the intensities of the activated voxels in the SI depend on the noise level and on the number of data points in the measured time series. Hence, even if the task-induced MR signal change is several percent, the signal-to-noise ratio (SNR) of the SI may be low.

Segmentation of noisy images is improved in many applications by utilizing spatial contextual information. Especially Markov random field (MRF) models are widely used. The main assumption behind most contextual segmentation methods is that the intensity distributions of different classes (e.g. the classes of the activated/non-activated voxels) are known a priori, or that the distributions can be estimated from the data. The goal is to find the most probable segmentation given the measured data and prior information. In this work, contextual segmentation is used in a different and new way. It is studied how the contextual segmentation and hypothesis testing can be combined so that the distributions of the activated voxels are not needed. A contextual clustering method based on the MRF model and iterated

[1] A voxel is the 3-D counterpart to a pixel, i.e. any of the small discrete volume elements that together constitute a 3-D image.

conditional modes algorithm (Besag, 1986) is developed and tested using simulated data and measured fMRI data. During an initialization step, the voxels are classified into activated and non-activated voxels by thresholding the SI. After the non-contextual initialization, the voxels are re-classified by using simultaneously both the SI values and classification information from the adjacent voxels. Information from larger neighborhoods is incorporated by iterating the classification. Although the algorithm is used for fMRI statistic images, it should be possible to use the methodology in other similar applications, too.

In summary, the goals of the present work are:

- to develop a computationally efficient fMRI activation localization and delineation algorithm, which utilizes information from the spatial neighborhood of each voxel but does not require the modelling of the activations,
- to evaluate the algorithm,
- to present some methodology and tools for comparing, combining and visualizing multimodal data.

This thesis is organized as follows. Imaging modalities related to this work are introduced in section 2. Contextual segmentation, MRF models and energy minimization in segmentation are discussed in section 3. The developed contextual clustering algorithm is introduced. In section 4, the frequently used fMRI analysis methods are reviewed and the main results from the use of contextual clustering in fMRI data analysis are presented. Multimodal and visualization aspects are discussed in section 5. Some concluding remarks are given in section 6. Section 7 contains short summaries of the publications of this thesis.

2 Medical imaging modalities

2.1 Magnetic resonance imaging

Magnetic resonance imaging (MRI) (Lauterbur, 1973; Wolbarst, 1993) is based on the nuclear magnetic resonance (NMR) phenomenon and, in turn, on the absorption and emission of energy in the radio frequency (RF) range of the electromagnetic spectrum. The discussion below is restricted to the imaging of protons, which are the most relevant nuclei in medical imaging. When placed in a magnetic field of strength B_0, protons will be aligned with their magnetic moments either parallel (lower-energy spin state) or antiparallel (higher-energy spin state) to the field. However, slightly more than half of the nuclei will be aligned in the lower-energy spin state creating a net magnetization for a population of protons. A proton with a net spin can absorb a photon of angular frequency ω_0. The Larmor frequency ω_0 depends on the gyromagnetic ratio γ of the given nucleus and B_0:

$$\omega_0 = \gamma \cdot B_0. \tag{1}$$

For hydrogen protons, $\gamma/2\pi = 42.58$ MHz / T. The protons are excited with an RF pulse. Soon after the photon absorption, the nuclei will re-emit some of the absorbed energy in the form of radio signals at Larmor frequency. In MRI, the emitted signal is spatially encoded by spatially varying magnetic fields created by gradient coils. Hence, different frequency components of the detected signal correspond to different locations of the source signal and spatial images are obtained by performing an inverse Fourier transformation. The original frequency domain signal space is called k-space. In practice, only a thin slice of the object under imaging is excited at a time using a slice selection gradient in the presence of a frequency-selective RF pulse. A volumetric image is constructed by combining the slice images.

In the classical view of nuclear magnetic resonance phenomenon, the net magnetization moment vector of the population of protons makes an angle with the direction of the external magnetic field (z-axis) after the RF excitation pulse. Immediately after the RF excitation pulse, the protons are in phase and give rise to the precessing transverse net magnetization. The time constant that describes how the z-component of the net magnetization vector returns to thermal equilibrium is called the spin-lattice or longitudinal relaxation time, T_1. Longitudinal relaxation is caused by a fluctuating magnetic field and exchange of energy between the spins and the lattice. The time constant that would describe the return to the equilibrium of transverse magnetization, M_{xy}, in the absence of magnetic field inhomogeneities, is called spin-spin or transverse relaxation time, T_2. The transverse relaxation is caused by longitudinal relaxation and spin-spin interactions leading to spin dephasing in the population of protons. Relaxation time T_2^* includes the effect of magnetic field inhomogeneities to the transverse relaxation time. By varying the sequence of the RF pulse applied and collected, different types of images, e.g. T_1-, T_2- or T_2^*-weighted, can be obtained. The clinical usefulness of MRI is based on the fact that relaxation times are tissue-type-sensitive. The contrast in gradient echo sequences arises from T_2^* effects, whereas spin echo sequences reflect T_2 effects (Kennan, 2000).

2.2 Functional magnetic resonance imaging

In the broad sense, the term functional MRI (fMRI) may mean any MR imaging technique used to study function in a human or an animal. In this work, fMRI refers to the detection of

hemodynamic changes associated with neural activity. The activation studies based on regional differences in oxygenated blood (BOLD contrast) (Kwong et al., 1992; Ogawa et al., 1990, 1992), are likely to be the most common fMRI technique. BOLD fMRI is discussed in more detail below. Perfusion MRI, which is the other main type of functional MRI, is based on the intravenous injection of a magnetic compound (Belliveau et al., 1990, 1991; Rosen et al., 1991) or arterial spin-labelling (Williams et al., 1992). Perfusion MRI provides extensive information on the capillary level tissue hemodynamics ranging from cerebral blood volume (Belliveau et al., 1990) and cerebral blood flow (Østergaard et al., 1996b,a) to the intravoxel distribution of flows (Østergaard et al., 1999). In the rest of this thesis, the term "fMRI" refers to activation studies based on BOLD.

Biophysics and physiology of BOLD-based fMRI

BOLD (blood oxygenation level-dependent) fMRI (Ogawa et al., 1990) is based on the difference in magnetic properties of deoxyhemoglobin and oxyhemoglobin (Thulborn et al., 1982), and on the local changes in the blood deoxyhemoglobin concentration during electrical neuronal activation. The paramagnetic deoxyhemoglobin, unlike the diamagnetic oxygenated hemoglobin, distorts the local magnetic field on a microscopic scale. Blood T_2 is predominantly determined by the oxygenation state of hemoglobin (Thulborn et al., 1982). The T_2 effect is caused by local magnetic field variations around the erythrocytes and water diffusion in these fields. T_2^* effects include T_2 effects but also the time-reversible dephasing of spins that is caused by the spatial distribution of the magnetic field within a voxel.

All relationships between neuronal activity, blood flow and oxygenation are not fully understood, but the process can be outlined as follows (Turner and Ordidge, 2000). First, some specific areas of the brain start to perform a task. Neuronal and metabolic activity, and the rates of oxygen and glucose usage increase in the activated areas. At this stage, the blood oxygenation decreases in the capillaries supplying the tissue and it may be possible to detect a small drop (early negative response) in the MR signal. Vasodilatory compounds are released at an increased rate and moved to the capillaries and resistance arterioles as long as the electrical activity persists. The resistance arterioles are dilated and blood flow increases in the resistance arterioles and in the capillary bed supplied by the arterioles. Also the capillaries dilate and oxygen supply to active tissue exceeds the demand. Blood oxygenation increases in capillaries and venules draining them, leading to the decreased concentration of deoxyhemoglobin. Blood volume increases in the venous bed. If the enhanced neuronal activity continues, vascular and metabolic changes reach equilibrium in 1–3 min. When the neuronal activity returns to baseline the blood flow also returns to baseline, but the blood volume in the draining venules remains elevated for 30–60 s.

It is worth noting that although the activation localization in the BOLD fMRI is based on the detection of relative signal changes, the measurements of the BOLD signal allow quantification of various parameters. These include the change in transverse relaxation rates during activation (Constable et al., 1993), the size of the blood vessels (Ogawa et al., 1993) and determination of the oxygen extraction ratio of a tissue (Oja et al., 1999b).

Spatial and temporal resolutions of BOLD fMRI

The spatial resolution of fMRI is determined by scanner hardware, physiological limits and ultimately hemodynamic limits. High spatial resolution in fMRI requires both an adequate signal-to-noise ratio (SNR) and contrast-to-noise ratio (CNR) (Kim et al., 2000). In MRI, the SNR is proportional to the voxel volume. At 1.5 T, voxel sizes of about 3–5 mm are typically used for fMRI. By using higher magnetic fields, better SNR can be obtained and the voxel size reduced. The SNR can also be increased by using surface coils if only specific regions of the brain are studied (Cohen et al., 1994). However, ultimately the spatial resolution of fMRI is restricted by the fact that fMRI does not measure neuronal activity directly. The measured BOLD signal includes components from the blood oxygenation changes in draining veins, which limits the spatial resolution of the BOLD fMRI (Lai et al., 2000). Several methods have been proposed to reduce the loss of spatial resolution caused by draining veins. These include the methods based on the use of MR angiography, the paramagnetic property of deoxyhemoglobin, the temporal phase of the fMRI signal time course, velocity dephasing gradients and the phase angle of the complex-valued fMRI time series (Lai et al., 2000; Menon, 2002). The utilization of an early negative response or the use of a differential imaging technique may enable even submillimeter resolutions (Menon, 2001).

The temporal resolution of fMRI is determined by the scanner hardware, used pulse sequences, neuronal-hemodynamic coupling, variability therein, and the question being asked (Bandettini, 2000). The minimum time between successive image acquisitions is about 100 ms, but the collection of a multi-slice volumetric EPI data set requires typically a repetition time of about 2 s (Bandettini, 2000). Activations following stimuli of about 30 ms have been detected. On the other hand, the fastest on-off rate of a stimulus in which the signal amplitude is not compromised is about $8 + 8$ s (Bandettini, 2000).

Noise and artifact sources of fMRI

In most MR imaging, the sources of noise include thermal noise from the subject, receiver coil, preamplifiers and other electronics, and quantization noise from the analog-to-digital conversion. Bulk head movement is likely the best known source of artifacts in fMRI. Respiratory effects, cardiac effects, CSF fluctuations and eye movements are important sources of physiological noise (Jezzard, 2000). Respiration-related artifacts, caused by small magnetic field shifts or head motion, may be serious especially if the used fMRI paradigm has a period similar to the respiratory period. Cardiac-related effects are mainly brain tissue pulsations caused by cerebral blood volume and pressure fluctuations, and inflow of fresh blood spins into the slice of interest. Biswal et al. (1995) reported slow signal fluctuations (frequencies < 0.1 HZ), which they explained by a manifestation of functional connectivity of the brain. Scanner instabilities may also be a major cause of low-frequency drifts in the signal (Smith et al., 1999). Endogenous neural activations also cause BOLD responses with spatial and temporal dimensions. Non-physiological artifacts include shape distortions, signal losses (drop-outs) and ghosting artifacts (Turner and Ordidge, 2000).

Fast MRI methods

Fast MR imaging techniques include fast low-angle shot (FLASH) imaging (Frahm et al., 1986), RARE (Hennig et al., 1986) and echo planar imaging (EPI) (Mansfield, 1977). In EPI, only one RF excitation pulse is used to generate data that is sufficient to fill the k-space. Functional MRI studies of this work were made using a gradient-echo EPI sequence with a rectilinear trajectory in the k-space, which is probably the most popular fMRI sequence. Variations of the used EPI technique include the spiral k-space sampling technique, echo-volumar imaging (Mansfield et al., 1985) and the principle of echo shifting with a train of observations (PRESTO) technique (Liu et al., 1993).

2.3 Other functional imaging or measurement techniques

Magnetoencephalography (MEG) is the recording of magnetic fields produced by electrical activity in the brain (Cohen, 1972; Hämäläinen et al., 1993). Superconducting magnetometers (SQUIDS) are used to measure the very weak magnetic fields in a magnetically shielded room. In most cases, the goal of the data analysis is to estimate the region where the source of the activity seen in the signals originates. In other words, a current distribution that would yield the measurements is calculated. A frequently used model of the source is the equivalent current dipole (ECD) model. Other solutions to this non-unique inverse problem include multipole expansions and distributed current sources (Hämäläinen and Nenonen, 1999). While fMRI gives indirect information on slow functional processes, the time resolution of MEG is much better. On the other hand, due to the difficulties and non-uniqueness of the inverse problem in MEG, the spatial localization accuracy of fMRI is generally better.

Electroencephalography (EEG) measures electric potential differences on the scalp produced by brain activity. Electric potentials are often affected by inhomogeneities in the head (Hämäläinen et al., 1993). Emission tomography methods (PET, SPECT) acquire information on the concentration and distribution of radionuclides introduced to the patient's body. The spatial resolution of SPECT ranges from 6 to 8 mm, whereas the resolution of PET is about 4 mm (Volkow et al., 1997). The temporal resolution of PET is about 45 s and of SPECT > 60 s (Volkow et al., 1997). Like fMRI/MEG/EEG, the emission tomography methods can be used to asses regional brain function but they are additionally useful in measuring biochemical components of neurotransmission (Volkow et al., 1997). Near-infrared (NIR) imaging, or (laser) optical imaging, is based on the modelling of the absorption and scattering of the near-infrared light in tissue (Villringer and Chance, 1997). In the method, the intensity and the mean time-of-flight of photons through the tissue are measured at different points on the boundary. The measured data can be used to reconstruct images of the changes in the optical properties of the tissue. NIR imaging utilizes the coupling between neuronal activity and optical properties of the brain.

A literature search using the MEDLINE / PubMed database (U.S. National Library of Medicine, http://www.nlm.nih.gov/) was done to estimate the relative change of (neuro-) fMRI, MEG, EEG and NIR publications from 1990 to 2000. For the results, see Fig. 1. The search was restricted to title words. Most frequent expressions of techniques were used, for example fMRI-related publications were searched using the expressions "fMRI", "functional AND MRI" and "functional AND magnetic AND resonance AND imaging". To reduce the number of false hits

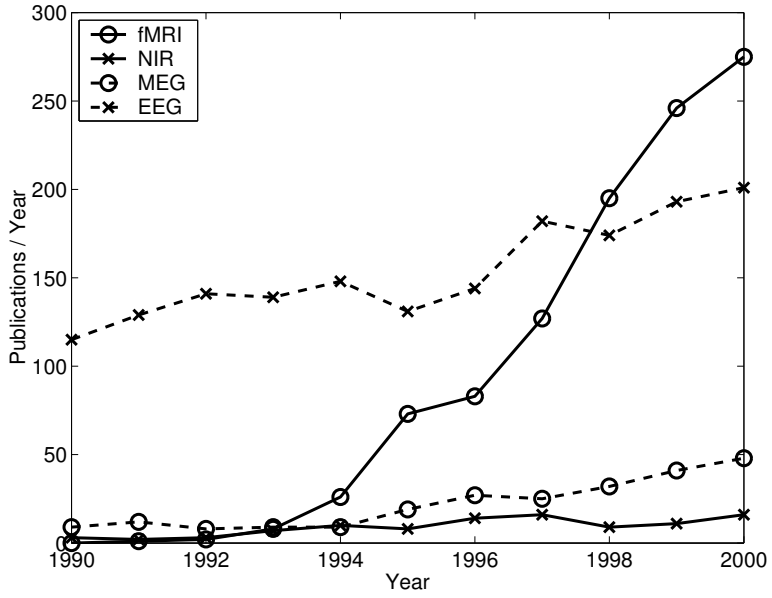

Fig. 1: *Increase of MEG, EEG, fMRI (neuro) and NIR (near-infrared) imaging-related publications in the MEDLINE/PubMed database during the 90s. The presented values are only relative – the actual number of publications is higher because the search was restricted by the keywords in titles.*

it was additionally required that brain- and activity/stimulus-related words existed anywhere within the records[2]. Naturally, the searches were capable of finding only a subset of all related publications. However, the results clearly show how the fMRI was virtually unknown at the beginning of 90s but in a few years changed to one of the most widely used brain function imaging methods.

[2]The exact Boolean search expressions were:
NIR: ((NIR[Title Word] OR (near[Title Word] AND infrared[Title Word]) OR optical[Title Word]) AND (imaging[Title Word] OR tomography[Title Word] OR topography[Title Word])) AND (neural OR brain OR cortex) AND (activity OR activation OR stimulus OR stimulation OR stimulated)
fMRI: fMRI[Title Word] OR (functional[Title Word] AND MRI[Title Word]) OR (functional[Title Word] AND magnetic[Title Word] AND resonance[Title Word]) AND (neural OR brain OR cortex) AND (activity OR activation OR stimulus OR stimulation OR stimulated)
MEG: (MEG[Title Word] OR magnetoencephalography[Title Word] OR magnetoencephalographic[Title Word] OR magnetoencephalogram[Title Word]) AND (neural OR brain OR cortex) AND (activity OR activation OR stimulus OR stimulation OR stimulated)
EEG: (EEG[Title Word] OR electroencephalography[Title Word] OR electroencephalographic[Title Word] OR electroencephalogram[Title Word]) AND (neural OR brain OR cortex) AND (activity OR activation OR stimulus OR stimulation OR stimulated)

3 Segmentation methods related to this work

By definition, segmentation means that an image is divided into non-overlapping (disjoint) objects in a meaningful way. Classification of each pixel or voxel of an image to one of the possible classes results in a segmented image. The number of different segmentation methods developed for medical images is huge. Some of the methods used in medical imaging were reviewed by Clarke et al. (1995) and by Acharya and Menon (1998). There are also several ways to classify the methods. One way is to divide the methods into non-contextual and contextual methods. In non-contextual methods, the voxel's classification does not depend on the measurement values of other voxels. A voxel is classified using only the measurement vector of the voxel under consideration. In the case of one-channel data, this is called one-level or multi-level thresholding. Contextual methods utilize information from other voxels, especially from the adjacent voxels. Another criterion divides segmentation methods into those that use an a priori model about the expected segmentation and those which do not. Geometry-driven methods use an a priori geometric model, which is deformed using edge information and elasticity constraints [for a review see e.g. Acharya and Menon (1998) and for an application see Lötjönen et al. (1999)]. The Markov random field models (MRF) are another approach to incorporate a contextual a priori model to the segmentation. The idea behind MRF models is outlined in the next subsection.

3.1 Markov random field-based segmentation

It is usually reasonable to assume that the distribution of class labelling at a voxel is conditioned on the class labels in the other voxels. Especially, it is likely that the true classification of nearby voxels is strongly correlated. This prior assumption can be modelled by Markov random fields (MRFs) (Besag, 1974; Geman and Geman, 1984), which are widely used in segmentation and noise reduction tasks. Besag (1986) introduced the iterated conditional modes (ICM) algorithm that is a computationally efficient method to carry out MRF-based segmentation. A similar algorithm was used by Kittler and Pairman (1985) to identify clouds. What is important to note is that these algorithms use both the measurement value of a voxel and classification information from the neighborhood simultaneously. Information from larger neighborhoods is incorporated by iterating the classification. The method developed in this thesis follows these ideas and is closely related to the ICM algorithm. Pappas (1992) presented a general MRF-based segmentation algorithm that took into account local intensity variations by an iterative procedure involving averaging over a sliding window whose size decreased as the algorithm progressed. Liang et al. (1994) segmented brain images using a Markov random field prior and 3-channel data including T_1-, T_2- and P_D-weighted 2-D MR images. Unlike in many other papers, the number of classes was estimated from the data. Park and Kurz (1996) developed a general MRF-based image enhancement algorithm and found that it outperformed e.g. the median filter. Held et al. (1997) described a fully automatic 3-D segmentation technique for brain MR images. Implementations based on simulated annealing and ICM were presented. Difference to the method by Liang et al. (1994) was that also intensity inhomogeneities and non-parametric intensity distributions were taken into account, but the classes were pre-determined. Rajapakse et al. utilized a 3-D MRF model in the segmentation of single-channel magnetic resonance (MR) cerebral images (Rajapakse et al., 1997; Rajapakse and Kruggel, 1998). Their method was also

adaptive to intensity inhomogeneities, but in addition MRF-parameters were estimated from the data. Also Kim and Paik (1998) presented an unsupervised segmentation method for MR images. Their method was based on an adaptive version of the ICM algorithm, and even the size of the window for parameter estimation was chosen using the data. Descombes et al. (1998b,a) proposed reduction of noise from fMRI datasets using an MRF model. Van Leemput et al. (1999) described a fully automatic brain tissue classification method. In their approach, initialization is done using a digital brain atlas containing prior expectations about the spatial location of tissue classes. Thereafter, tissue classification including correction for MR signal inhomogeneities and parameter estimation is done in an interleaved manner by maximizing tissue likelihood in the presence of MRF-prior.

An MRF model defines interactions of different class values. Interactions are considered within some neighborhood. The neighborhood of a pixel or voxel consists of its closest pixels or voxels. In most cases, first-, second- or third-order neighborhoods are used. The first-order neighborhood consists of the four closest pixels in 2D and the six closest voxels in 3D. The second-order neighborhood consists of the eight closest pixels in 2D and the 18 closest voxels in 3D. The third order neighborhood in 3D additionally includes the eight corner voxels into the neighborhood. Another useful term is "clique". A clique is a set of pixels or voxels that are all neighbors of each other.

Mathematically the concept of the MRFs can be described as follows. Let $i = \{1, 2, \ldots, n\}$ index n sites (pixels / voxels) of an image I. Let x_i represent the classification of the site i and let x represent the classification of all sites. Let $\mathcal{N}_i$ be a neighborhood of site i. The random variable representing x is a locally dependent Markov random field if

$$p(x_i|x_{I\backslash i}) = p_i(x_i|x_{\mathcal{N}_i}), \tag{2}$$

where $I\backslash i$ refers to all sites of I excluding site i. A usual requirement is that the probability of any particular segmentation of the image is positive (positivity constraint): $x \in \Omega, p(x) > 0$, where Ω is the set of all possible segmentations. Then, according to the Hammersley-Clifford theorem [see e.g. Besag (1974)] the density of x is given by a Gibbs distribution:

$$p(x) = \frac{1}{Z}\exp[-\sum_{c\in C} V_c(x)]. \tag{3}$$

Here Z is a normalization constant whose value is not usually needed in segmentation. V_c is a potential function associated with clique c. The summation is over all cliques C. The higher the potential value of a clique configuration is, the less likely its existence is a priori. One difficulty in using Markov random fields lies in the determination of potential function V_c for different types of cliques. Often the potential functions are determined heuristically and the usefulness of the model is demonstrated by using test data.

The simplest but regularly used approach is to give non-zero potentials only to singletons (i.e. cliques consisting of only one voxel) and doubletons (cliques consisting of two voxels) [see e.g. Rajapakse et al. (1997); Rajapakse and Kruggel (1998)]. A drawback of this simplification is worth noting: the position information of neighboring class values is not utilized in contrast to the use of more complicated cliques (Park and Kurz, 1996). It is argued that these simple models are not well suited for segmentation as they cannot represent the "real world" (Morris et al., 1996). Especially with "true" values for potential values, the models do not seem to provide

enough "smoothing", but may delete fine structures. On the other hand, these models have been used successfully in many applications. The problems can be avoided at least partially by defining additional restrictions for the potential functions. The use of more complicated models [e.g. the line and fine structures preserving chien model with 3×3 cliques by Descombes et al. (1995)] in segmentation is rare, possibly due to the computational difficulties, which may be severe in 3D.

The potentials of the singletons (often expressed using α) reflect the a priori knowledge of the relative likelihood of the different classes. If the a priori likelihood of different classes is not used (e.g. the classes are assumed to be equally likely), the potentials of the singletons are set to zero. The potentials of the doubletons (β) are used to adjust the likelihood that neighboring voxels belong to different classes. One method is to set the potential to β if the voxels belong to different classes and otherwise to 0 or $-\beta$ [e.g. Besag (1986); Pappas (1992)]. Sometimes different potentials ($\beta_1, \beta_2, \ldots$) are defined to the first-order, second-order etc. neighbors [e.g. Rajapakse et al. (1997); Rajapakse and Kruggel (1998); Liang et al. (1994)]. Also possible different voxel dimensions in $x-$, $y-$, and $z-$directions can be taken into account by defining different interactions for different directions. Sometimes it is useful to order the classes and define the potentials to utilize this order information. For example, a larger potential could be given for cliques consisting of white matter (WM) and cerebral spinal fluid (CSF) voxels than for cliques consisting of gray matter (GM) voxels in place of CSF voxels. This would reflect prior knowledge that GM voxels are often located between WM and CSF voxels. Another example is noise reduction using an MRF model. In this case, the potential function can be defined to be a function of difference of intensity values inside a clique (Park and Kurz, 1996). It is worth noting that an MRF model is often not expected to be an accurate model of the true image itself but a tool to utilize contextual information. Hence, even if the Markov a priori model is not accurately determined, its use may significantly improve segmentation results.

3.2 Goals of segmentation

A frequent goal of segmentation is to choose the most probable segmentation x (maximizing a posteriori probability, MAP segmentation) given the measurement data and the available a priori information. Let vector z contain the measurement values, or some other features, of voxels. Thus, by Bayes' theorem x maximizes the probability

$$P(x|z) \propto p(z|x)p(x). \tag{4}$$

Another goal of segmentation might be to maximize the marginal posterior probability (MMP) at each voxel i. That is, to maximize

$$P(x_i|z) \propto \sum_{x_{I\setminus i}} p(z|x)p(x). \tag{5}$$

This is equivalent to the minimization of the expected number of erroneously classified voxels and can be seen as an approximation to MAP. The x_i's can be estimated using the Gibbs sampler (Geman and Geman, 1984).

It is worth noting that the MAP (or MMP) segmentation requires realistic models about the data and the estimation of the model parameters. For example, the models used for the

segmentation of brain MR images include the non-contextual finite Gaussian mixture model and the contextual Gaussian hidden MRF model (Zhang et al., 2001). Typically, the unknown parameters are the means and variances of the Gaussian distributions and MRF parameters like singleton and doubleton interaction parameters. The inclusion of bias field and partial volume models introduces additional unknown parameters. The determination of the parameters using either training data or the actual data is the central issue of many publications. Several methods like the expectation-maximization algorithm (Dempster et al., 1977; Van Leemput et al., 1999; Zhang et al., 2001) have been proposed to estimate the parameters. Estimation of the model parameters is often carried out in an iteratively manner simultaneously with the energy minimization (see the next subsection) algorithm. We have adopted an alternative approach, namely the classification by hypothesis testing, not requiring the estimation of parameters.

When the voxels of an image are classified into two classes, ω_0 and ω_1, there are two basic types of errors:

- a voxel of class ω_0 is erroneously classified to class ω_1 and
- a voxel of class ω_1 is erroneously classified to class ω_0.

Segmentation by hypothesis testing means classification of the voxels into two classes so that one of the classes is defined as a *null* class. A voxel is classified to the alternative, or rejection, class if the null hypothesis is rejected. The null hypothesis is rejected if the probability for the test statistic, or a higher one, to occur by chance assuming that the null hypothesis is true is smaller than a predefined α-level. Segmentation by hypothesis testing can be used if the intensity distribution of the null class is known. The difference between MAP- and testing-based classification is illustrated in Fig. 2. Voxel classification based on hypothesis testing is widely used in fMRI data analysis because

- the distribution of non-activated voxels can be approximately characterized but the distribution of activated voxels is unknown,
- the classification of a non-activated voxel to the activation class is considered a more serious error than the classification of an activated voxel to the non-activation class, and
- the significance (p-) values of the found activated regions are often needed to report the significance of the findings.

Hypothesis testing is often performed on each voxel separately. Segmentation methodology and contextual information are seldom used in testing approaches. Generally speaking, the use of information from other voxels prevents accurate statistical voxel-specific inferences. However, by properly choosing the segmentation algorithm the advantages may be more important than the drawbacks.

3.3 Minimization of energy function

The a posteriori probability of segmentation x can be written as $P(x|z) \propto \exp - U(x)$, where $U(x)$ is called the energy function. Maximization of the a posteriori probability is then equivalent to the minimization of energy function $U(x)$. In practice, the minimization algorithm determines the labelling of the voxels and is occasionally called the labelling algorithm. A

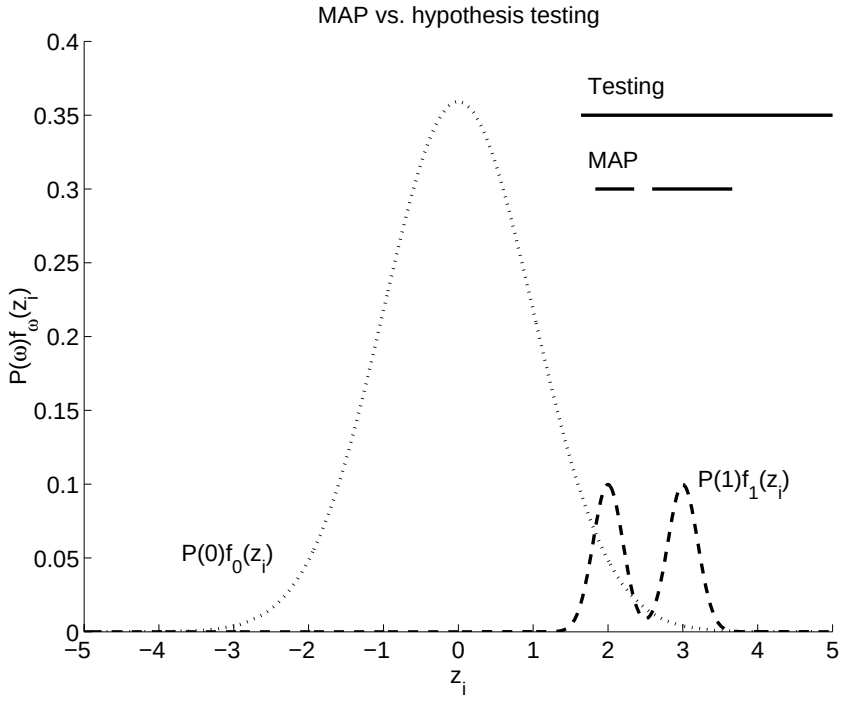

Fig. 2: *Schematic illustration of differences between MAP- and hypothesis-testing-based classification when only intensities (no spatial information) are used. The dotted line represents the density f_0 of a background class multiplied by its a priori probability $P(0) = 0.9$, the dashed line the density f_1 of an alternative class multiplied by its a priori probability $P(1) = 0.1$. Values classified to the alternative class with MAP and testing techniques are shown in the right upper corner of the figure. In MAP classification, voxel i is classified into the alternative class whenever $P(1)f_1(z_i) > P(0)f_0(z_i)$. This requires a knowledge (usually estimation) of f_0, f_1 and their a priori probabilities. In classification based on a hypothesis testing, a voxel is classified to the alternative class when the probability for the value of z_i, or a higher one, by chance, and assuming the background class, is small enough. This requires knowledge of f_0 only.*

simulated annealing (SA) algorithm is widely used to find the minimum of the energy function [see e.g. Kirkpatrick et al. (1983); Geman and Geman (1984); Lakshmanan and Derin (1989); Descombes et al. (1998b,a); Rajapakse and Piyaratna (2001)]. The main benefit of the SA algorithm is that it converges toward the global minimum of the energy function and does not depend on the initialization (Geman and Geman, 1984). This is achieved by allowing an increase of the energy function with a probability that is related to the parameter referred to as temperature, T_e. To adhere to the theoretical properties of convergence, the temperature T_e must be decreased logarithmically. The final classification after a large number of cycles is considered to be an energy minimum and an MAP estimate of the classification. The main downside of the SA algorithm is its huge computational demands.

One difficulty with Markov random field models is the phenomenon known as phase transition, which creates images consisting of only one class. Besag (1986) proposed the iterated conditional modes (ICM) algorithm for the minimization of the energy function. Originally, the ICM was proposed as an approximation to MAP estimation, although later it was also considered to overcome the phase transition problem. In the ICM algorithm, the class label of

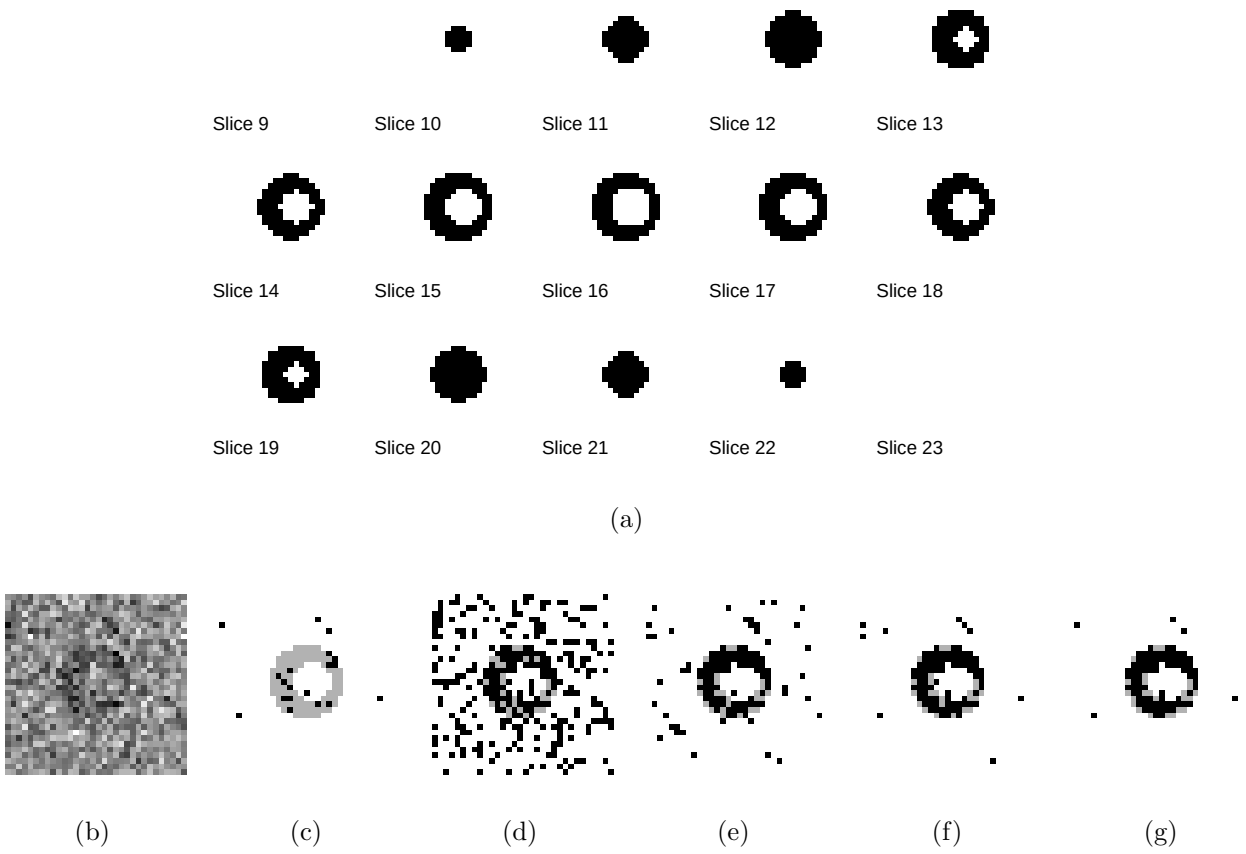

Fig. 3: *Detection of a simulation object from a noisy background. (a) Fifteen spatial levels of a simulation object* $32 \times 32 \times 32$ *voxels in size. All other levels are empty. (b) Slice* 15 *of the simulation object added to a noisy background. The noise follows* $N(0, 1)$*; mean of the object is* $\mu = -1.5$*. (c) A thresholded image with a false-positive rate FPR* ≈ 0.006*;* $T \approx -2.52$*, (d) an initialization image for contextual clustering* $T_{cc} \approx -0.806$*, and* $\beta = T_{cc}^2/6$*, (e) contextual clustering after the first cycle, (f) contextual clustering after the second cycle, (g) contextual clustering after the* 10^{th} *cycle (convergence), FPR* ≈ 0.006*. In (c)–(g), the object voxels erroneously classified to the background are shown in light gray. A version of the contextual clustering for negative object values was used. Source: Publication I.*

site i is updated so that the a posteriori probability

$$P(x_i|z, \hat{x}_{I\setminus i}) \propto f(z_i|x_i)p_i(x_i|\hat{x}_{\mathcal{N}_i}) \tag{6}$$

is maximized (Besag, 1986). Here $f(z_i|x_i)$ is the conditional density of the observed z_i with given x_i. The maximization is applied to each voxel in turn or to all voxels simultaneously. The ICM algorithm, or its variants, have been used widely to minimize the energy in MRF-based segmentations [see e.g. Liang et al. (1994); Kim and Paik (1998); Zhang et al. (2001)].

The Gibbs sampler (Geman and Geman, 1984) is a technique used to sample realizations from the posterior distribution of x. The sampling is started with some initial segmentation. Each pixel is processed in turn. In the basic version, the new classification x_i for pixel i is

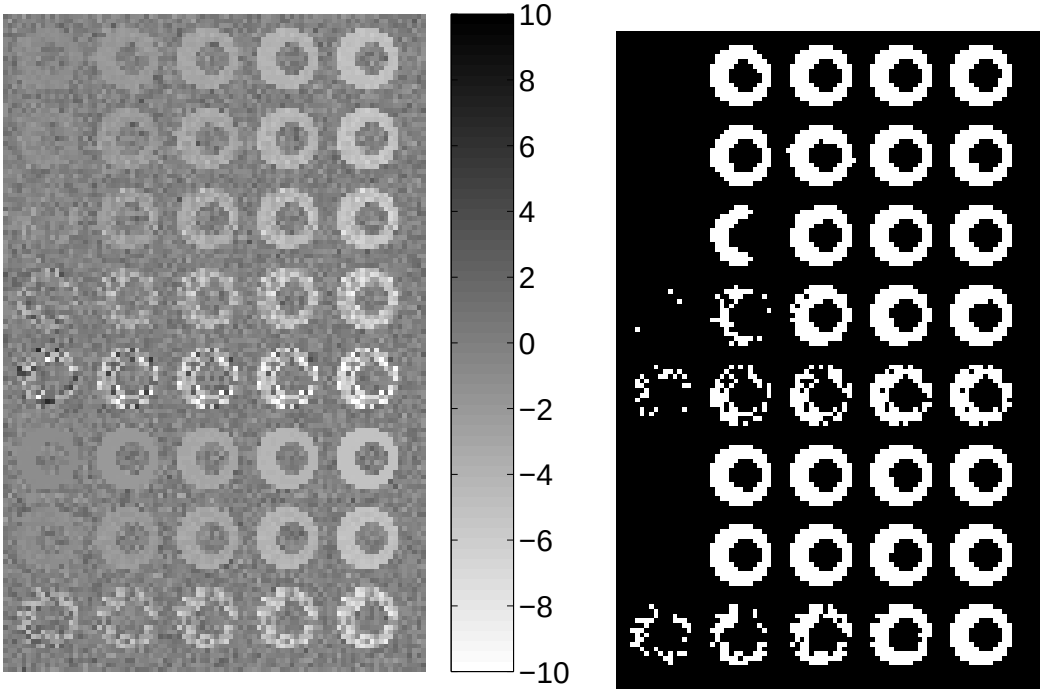

(a) (b)

Fig. 4: *Contextual clustering of an image containing multiple objects. (a) The source image. The voxel intensities on the object regions follow different distributions with different means and variances, (b) the segmentation result. The segmentation was obtained using parameter values* $T_{cc} \approx -1.48$, $\beta \approx 0.37$. *Source: Publication I.*

chosen with probability

$$P(x_i|z, x_{I\setminus i}) \propto f(z_i|x_i)p_i(x_i|x_{\mathcal{N}_i}). \tag{7}$$

MMP estimation can be performed by running the Gibbs sampler several cycles and counting the most frequent class for each voxel after a burn-in period, which removes the effects of the initial sampling values.

Dubes et al. (1990) compared the ICM, SA and MMP methods. The ICM method was found to perform consistently well and to be the most robust on images corrupted by correlated noise. It was noted that although the SA is theoretically guaranteed to find a globally optimal segmentation, it can fail in actual problems because compromises are needed to overcome the computational burden. In addition, the ICM was a few orders of magnitude faster than the SA. The MMP implemented using the Gibbs sampler required more computation than the ICM but far less than the SA.

3.4 Approach used in this thesis

In this work, we have developed a method to perform segmentation into two classes, a background class ω_0 and an alternative class ω_1, by hypothesis testing simultaneously utilizing neighborhood information. It is assumed that the true distribution of class ω_0 voxels is known to be the standard normal $N(0, 1)$, possibly after the transformation of the variables. The

Contextual clustering algorithm

Contextual clustering algorithm, which segments an image into background (ω_0) and object regions (ω_1), is presented. The voxel intensities of the background are assumed to be drawn from standard normal distribution.

1 Define decision parameter T_{cc} (positive) and the weight of neighborhood information β (positive). Let N_n be the total number of voxels in the neighborhood [a]. Let z_i be the intensity value of voxel i.

2 Initialization: Classify voxels with

$$z_i > T_{cc} \tag{8}$$

to ω_1 and other voxels to ω_0. Store the classification to variables C_0 and C_1.

3 For each voxel i, count the number of voxels, u_i, belonging to class ω_1 in the neighborhood of voxel i. Assume that the voxels outside the image volume belong to ω_0.

4 Classify voxels with

$$z_i + \frac{\beta}{T_{cc}}(u_i - N_n/2) > T_{cc} \tag{9}$$

to ω_1 and other voxels to ω_0. Store the classification to variable C_2.

5 If $C_2 \neq C_1$ and $C_2 \neq C_0$, copy C_1 to C_0, C_2 to C_1 and return to step 3, otherwise stop and return C_2.

Note: The presented form of the algorithm detects positive deviations from the standard normal distribution. If negative deviations are to be detected, T_{cc} should be chosen to have a negative value and "$>$" should be replaced with "$<$" in Equations (8) and (9).

[a] All experiments in this work have been conducted using the 3rd-order 3-D neighborhood, i.e. $N_n = 26$

distribution of class ω_1 values is unknown. The classification could be done by a one-sided hypothesis test, accepting the null hypothesis that a voxel belongs to ω_0 whenever the voxel intensity z_i is smaller than a predefined threshold T_{cc}, and otherwise rejecting the null hypothesis and thus classifying the voxel to class ω_1. In order to utilize neighborhood information, an artificial distribution for class ω_1 is introduced, $N(2T_{cc}, 1)$. That way the maximum likelihood (ML) classification of each voxel into either ω_0 or ω_1 will produce the same result as the one-sided hypothesis test. Then a Markovian random field model on the classification is added, and the classification is estimated as a local maximum in the posterior probability, thus giving a neighborhood-information-added analog to the one-sided hypothesis test. A 3-D MRF model with pair-wise interactions and a third-order neighborhood is used. The potential function is defined as $V_c = 0$ if both voxels of a doubleton belong to the same class, and otherwise as $V_c = \beta$. Minimization of the energy function is done following ICM style minimization, because

- ICM is computationally efficient,
- the results depend only on the local characteristics of the data, and
- there is some evidence (Dubes et al., 1990) on the good robustness against spatial corre-

lations in the noise term.

We will call the segmentation carried out using the ideas presented a "contextual clustering". Its steps are summarized in the box, for details of the derivation see Publication I. Segmentation of a single object from random noise is illustrated in Fig. 3. Segmentation of several objects following different distributions is shown in Fig. 4. It is worth noting that the algorithm measures deviation from the background only (i.e. no information about object distributions is used). In addition, apart from the immediate neighborhood of object voxels, type I error probabilities are determined by the parameters of the algorithm (T_{cc} and β) only.

The essential difference between the ICM algorithm (or MAP estimation) and the proposed algorithm is worth noting. In the ICM, relative a posteriori probabilities for a voxel belonging to classes ω_0 and ω_1 should be estimated. A voxel is classified to a class whose a posteriori probability is the highest. This requires a priori information about the statistical properties of both classes and parameter estimation. In our approach, only the statistical properties of background class ω_0 are used. Loosely speaking, a voxel is classified to ω_1 if the values of the voxel and the "surrounding" voxels differ enough from the distribution of class ω_0. For this reason, the need for the modelling of activation distributions is avoided. In the derivation from the ICM, the "real" activation class was replaced with an artificial test class. The mean of the test class and the interaction between neighboring voxels are set so that a desired overall or voxel-level type I error rate is achieved, i.e. the mean and MRF parameters no longer represent the characteristics of the true image. We emphasize that the replacement is a heuristic step. Hence, relatively extensive tests were conducted in Publications I–III. Main results of the tests are presented in section 4.

4 Data analysis

4.1 Acquisition of data and goals of fMRI data analysis

In fMRI activation studies a stimulus is given to a subject or the subject is asked to perform a task. Time series of MR images are recorded and analyzed. In epoch-based, or block-based fMRI, blocks of different states (e.g. control and stimulus) are alternated and the images of different states are compared. Each block typically consists of several images. Too short blocks are inefficient due to the slowness of the hemodynamic response. On the other hand, too long blocks should be avoided due to baseline fluctuations, subject's movements and discomfort. Optimal block length and other parameters of the study designs are debated questions and out of the scope of this thesis.

In addition to epoch-type studies, fMRI can be used to study event-related activations (Buckner et al., 1996; Rosen et al., 1998). Event-related fMRI is used to study responses to short stimuli, e.g. to single words. Event-related task paradigms can be used to map hemodynamic changes lasting in the order of seconds or several hundreds of milliseconds. Event-related fMRI provides the ability to study the same paradigms in both fMRI and MEG (or EEG) sessions.

The number of articles related to the fMRI data analysis is large [see e.g. Lange (2000)]. Perhaps the most common goal of fMRI data analysis is to localize the brain areas responsible for the processing of the stimulus. In many approaches, the localization of fMRI activations consists of three phases:

1) Preprocessing of the data, possibly including motion correction and smoothing or noise reduction,

2) voxel-by-voxel computation of the statistic image (SI), also called a statistical (parametric) map, and

3) segmentation of the SI into activated and non-activated regions.

Phase 2) essentially reduces the 4-D spatio-temporal fMRI data into a 3-D spatial image by considering all time series separately. The values of the SI follow a known null distribution in non-activated voxels. Phase 3) is usually called a testing phase aiming to detect statistically significant activations from the 3-D SI. As will be later discussed, this phase is usually carried out so that the probabilities of false activation detection ("false-positive rates (FPR)") are controlled either at the voxel level or the overall (volume) level. The term "segmentation" is used here to emphasize that, at least implicitly, the ultimate goal is not only to obtain information about the location of activation centers but also to obtain other information like the shapes or sizes of the activations. The simplest approach to segment SI is to threshold it in a voxel-by-voxel manner. However, it is generally accepted that the truly activated voxels tend to form clusters, and methods to incorporate spatial information during step 3) have been developed. We shall describe later in this overview how the contextual clustering procedure described in section 3 can be used to perform phase 3).

This thesis will concentrate on the localization and delineation of activations. However, several other questions may be posed than just where the activation happened. Bayesian models with Markov Chain Monte Carlo posterior sampling seem useful in estimating many hemodynamic parameters, for example signal rise times or the impact of changing task demands

(Genovese, 2000; Gössl et al., 2001). Path analysis is used to quantify relationships between multiple brain regions (Bullmore et al., 1996b, 2000). The goal of time series clustering [see e.g. Baumgartner et al. (1997); Golay et al. (1998); Baune et al. (1999); Goutte et al. (1999); Ngan and Hu (1999)] is to partition the time series into clusters of similar time courses. Typically, time series clustering does not require prior assumptions about the shape of the expected time course.

Multivariate analysis, like singular value decomposition (SVD) and independent components analysis (ICA) (McKeown et al., 1998), take place on all voxels' time courses at the same time. SVD, or related principal component analysis (PCA), may be used to explore fMRI-signal structures without any a priori knowledge about the activation signal [e.g. Bullmore et al. (1996b); Lange (2000)]. As an example, Friston et al. (1994a) used SVD to extract a global representation of the hemodynamic response function.

4.2 Preprocessing of fMRI data

Reliable activation detection and the controlling of false-positive rates (FPRs) in fMRI activation detection requires modelling of noise. Noise can be divided into systematic and random noise. Optimal detection of activations requires a correct model for the hemodynamic response. Both the noise and hemodynamic response have temporal and spatial aspects.

The simplest approximation for the time courses of a non-activated voxel is that the intensity values are independently drawn from a Gaussian distribution with some mean μ and variance σ^2, constant over the experiment. In an approximation, the time courses are also spatially independent if the means are not considered. This white Gaussian noise model is often implicitly assumed in the widely used t-test methods. In practice, the intensity values of fMRI data are correlated in time and space. The amount of correlation may depend, e.g., on the size of voxels and the time of repetition. The number of false-positive detections may differ from the expected number of false positives if the correlations are not taken into account properly. In addition, the changes in the baseline level cause substantial difficulties in the data analysis. Spatial aspects are closely related to the activation detection phase and are hence deferred to subsection 4.4.

The primary reason for low-pass filtering in statistical analysis is to set the degrees of freedom of the data to a known level. In addition, running a filter whose width corresponds to the width of the signal increases detection sensitivity. Kruggel et al. (1999) compared a moving average filter, an FIR low-pass filter, an autoregressive filter and a Kalman filter with event-related data. The best sensitivity was determined for the moving average filter, closely followed by the temporal low-pass filter. However, the low-pass filter revealed a higher independence of the results in relation to the filter parameters. Zarahn et al. (1997) reported that temporal autocorrelation in spatially unsmoothed data is described well by a $1/f$ relationship, where f is frequency. In addition, they found that temporal smoothing of the noise data with low-pass filters in conjunction with the use of a general linear model (GLM) (Worsley and Friston, 1995) was advantageous in controlling FPRs.

Systematic noise, like drifts and fluctuations, may be caused, e.g., by scanner instabilities, scanner noise, motion artifacts, variations in blood pressure and respiratory or cardiac effects (Bandettini et al., 1998; Smith et al., 1999). A standard approach is to high-pass filter the time series or simply remove a linear trend. The high-pass filtering can be performed as a separate pre-processing step or it can incorporated to the linear model discussed later. Biswal et al.

(1996) described the use of finite impulse response (FIR) band reject digital filters in removing physiological fluctuations. Buonocore and Maddock (1997) developed an adaptive Wiener filter to suppress cardiac and respiratory structure noise in fMRI images. Skudlarski et al. (1999) found that removal of intensity drifts using high-pass filtering is beneficial to the efficacy of the analysis. Marchini and Ripley (2000) removed non-linear trends by using a simple running-lines smoother, which they found to be a reliable method.

A global nuisance signal can be partially taken into account by scaling the images, so that they all have the same global mean value. However, it is possible that much of the brain truly responds neurally to the experimental paradigm and that adjustment for the global signal leads to inferences about brain function based on artifact (Aguirre et al., 1998b). The global signal can also be included as a nuisance covariate into the GLM (Zarahn et al., 1997).

In order to optimize the sensitivity of activation detection, the hemodynamic response function (HRF) should be modelled accurately. It is generally known that the hemodynamic response is slow. After the onset of neural activation, it increases to a peak value during several seconds. Return to the baseline is even slower. Several models have been used for the HRF.

In using the Fourier transform technique, only the frequency of the activation needs to be known (Bandettini et al., 1993). The same is true when a linear combination of sine and cosine terms at the fundamental frequency of simulation is fitted (Bullmore et al., 1996a) to the data. These approaches are naturally limited to the periodic stimulus functions. A widely used approach is to use a model of a linear and time-invariant system, although it is generally known that the model is not precisely correct. For example Dale and Buckner (1997) demonstrated that the fMRI signal summated approximately linearly in visual stimulation experiments although subtle departures from linearity were observed. In the epoch-based experiments, the linearity is not as important issue as it is when short stimuli are repeated rapidly. In the linear model the response to an arbitrary input (stimulus) function is equal to the convolution of that input with the system's impulse response. Then, the observed fMRI signal $x(t)$ (without baseline) at time t in a discrete-time domain is given by

$$x(t) = \alpha \sum_s h(t-s)p(s) + \epsilon(t), \tag{10}$$

where α is the gain of the fMRI imaging process, $p(s)$ is the stimulus function, $h(t)$ is the impulse response function and $\epsilon(t)$ represents additive noise. Assuming that the effects of stimuli summate linearly, this equation can be applied not only to a single stimulus but also to cases where many stimuli are presented rapidly. The simplest model for the impulse response function is the delta function. Then $x(t)$ is modelled to be $\alpha + \epsilon(t)$ during a stimulus and $\epsilon(t)$ otherwise. A slightly more realistic approach is to add a delay of few seconds to the system. These models are implicitly used in the two-sample t-test. In more advanced approaches, the impulse response function is modelled by a gamma or Poisson density function (Friston et al., 1994b; Boynton et al., 1996; Cohen, 1997), a difference between two gamma density functions (Friston et al., 1998), a Gaussian function (Rajapakse et al., 1998), or an empirically derived function. Variation in the impulse response (e.g. variation in lag and and dispersion) can be modelled by a combination of basis functions or by a finite-impulse response (FIR) set. Choices for the basis function include a canonical response function and its derivatives (Friston et al., 1998), a Fourier set (Josephs et al., 1997) and gamma density functions (Dale and Buckner, 1997). The FIR sets do not assume any shape for the hemodynamic response, although it is

possible to include knowledge about the responses using restriction matrices (Burock and Dale, 2000). In the linear model, it is also possible to define different impulse response functions to different types of stimuli.

Movement correction and other geometrical transformations

Movement of a subject is considered to be one of the most serious problems in fMRI experiments. Movement may lead to decreased detection sensitivity or movement artifacts. Often the head of the patient or volunteer is fixed with a vacuum pillow during scanning. Also bite bars are used. However, small movements cannot be avoided. To remove the effect of head movements, several motion correction algorithms based on the internal properties of the data and either rigid or non-rigid models have been developed and used. The movement correction, as registration in general, encompasses several separate problems. These include the selection of a cost function, optimization of the cost function and interpolation of the data after the determination of the transformation parameters (Woods et al., 1992; Friston et al., 1996b; Eddy et al., 1996; Kim et al., 1999; Cox and Jesmanowicz, 1999; Jenkinson and Smith, 2001a).

Movement correction is an example of within modality, within subject registration procedure. Several other registration and transformation procedures are also needed in the analysis of functional data [see e.g. Jenkinson and Smith (2001b)]. In order to show activation maps on the top of high-resolution structural MR images, a between modalities within subject registration is widely used. In this case raw functional MR data (e.g. EPI) is registered with the structural images because the computed activation maps are not suitable for registration. In some cases, slice position and orientation information from the headers of image files can be used and registration can be avoided. There is also often a need to combine between modalities within subject, and between subjects within modality transformations in order to show the activation maps of different subjects on the top of one common reference image. Difficulty lies in the fact that substantial variation between anatomies exists. Generally, one of the subjects is chosen as a reference. Structural images of other subjects are elastically registered with the reference subject. Then the functional images of each subject are registered with the corresponding structural images of the subject. Finally, the two transformations are combined and activation maps are transformed to the coordinates of the reference structural image. Alternatively, some standard atlas, like the coordinate system of Talairach and Tournoux (1984), can be used as a reference coordinate system. This has the advantages that the results can be reported in standard generally known coordinates and compared easily with other studies. Additional references concerning the geometrical transformations include Pelizzari et al. (1989); Thompson and Toga (1996); Christensen et al. (1997); Ashburner et al. (1999).

4.3 Computation of statistic images

In the most basic fMRI analysis technique, the mean of images acquired during one condition is subtracted from the mean of images acquired during an alternative condition. Images obtained at the beginning of each epoch are generally discarded due to the delay in the hemodynamic response. However, the subtraction technique alone does not give information about the statistical significance of the difference. Instead of direct subtraction, statistic images (SIs) are preferred. In the SI, non-activated voxels follow a known null distribution. There are several

ways to compute such images.

The SI of t-statistic can be obtained from a subtraction image by normalizing it with the standard error estimate, i.e. using the methodology of standard Student's t-tests. The t-statistic has been used from the early days of fMRI (Constable et al., 1993). In the correlation analysis (Bandettini et al., 1993), correlation coefficients are calculated between the measured signal and an expected response function (reference signal) at each voxel. Thereafter, the calculated correlation coefficients are compared with the theoretical null distribution coefficients. Several variations exist. Kleinschmidt et al. (1995) used correlation coefficient maps with noise distribution reconstructed from the actual data. Kuppusamy et al. (1997) used a combination of cross-correlation and t-test images. An example of spectral density estimation methods is a non-parametric technique described by Marchini and Ripley (2000). The method was found to be more resistant to high-frequency artifacts than the usual time-domain approaches.

The t-test and the correlation test are special cases of the general linear model (GLM) (Friston et al., 1995). Usually, the GLM is written in matrix form:

$$x_i = Gb_i + \epsilon_i \tag{11}$$

Here x_i includes measured data for voxel i, G is called a design matrix, b_i is a vector of unknown model parameters, and ϵ_i is a vector of residuals drawn from a Gaussian distribution. The design matrix G models the experiment, e.g. the hemodynamic response (see section 4.2), baseline, and nuisance effects, like low-frequency components. The columns of G represent different parts of the model and each row represents one scan (3-D volume). If G is full rank, the least squares and simultaneously the maximum likelihood (ML) estimates of b are given by

$$\hat{b}_i = (G^T G)^{-1} G^T x_i, \tag{12}$$

where T indicates the transpose and -1 the inverse of a matrix. In the case that the data are convolved (smoothed) using a convolution kernel K, the GLM is written as

$$Kx_i = KGb_i + Ke_i. \tag{13}$$

Unbiased estimators for b_i, its variance and statistical significance were given by Worsley and Friston (1995). For example,

$$\hat{b_i} = (G^T K^T K G)^{-1} G^T K^T K x_i. \tag{14}$$

The primary goal of smoothing is to set the temporal autocorrelations to a known level so that SIs can be computed properly. An alternative approach to the temporal smoothing is to estimate and remove the actual autocorrelations (pre-whiten the data) (Bullmore et al., 1996a; Burock and Dale, 2000; Woolrich et al., 2001). Woolrich et al. (2001) found their pre-whitening approach to give valid statistics at the voxel level and to maximize estimation efficiency.

In order to test a specific effect at voxel i (e.g., is $b_{1,i}$ significantly larger than zero?), a t-statistic value is calculated. The t-statistic value is calculated by dividing a contrast (i.e. linear compound of the parameter estimates) by the estimated standard error at the voxel [for details, see Friston et al. (1995); Worsley and Friston (1995)]. When there is no specific effect at the voxel, the t-value is drawn from a null distribution, which is, in theory, a t-distribution. All t-statistic values displayed together form a t-statistic image. The t-statistic images can be

transformed to standard z-statistic images using the transformation $\Phi(t) = \Psi(z)$, where $\Phi(\cdot)$ is the t-distribution function and $\Psi(\cdot)$ is the cumulative standard Gaussian function. The knowledge about the null distribution enables the determination of voxels in which the specific effect is statistically significant. The next subsection covers this issue in greater detail. In addition to t-statistic, also an F-statistic is widely used with the GLM. An F-test can be used to assess the significance of a subset of basis functions. The F-test allows comparison of the different factors to the model.

Other statistics are used, too. For example, Bullmore et al. (1996a) presented a test statistic called a fundamental power quotient (FPQ). In the approach, an fMRI signal is modelled by the sum of a fitted sine wave and a cosine wave. The FPQ at a voxel is given by

$$FPQ = \frac{1}{2}\left[\left(\frac{\hat{\gamma}}{\hat{\sigma}}\right)^2 + \left(\frac{\hat{\delta}}{\hat{\sigma}}\right)^2\right], \tag{15}$$

where $\hat{\gamma}$ and $\hat{\delta}$ are estimates of the amplitude of a sine wave and a cosine wave, respectively, and $\hat{\sigma}$ is an estimate of the assumed common standard error of $\hat{\gamma}$ and $\hat{\delta}$. In theory, $2 \times FPQ$ has approximately the chi-squared null distribution with two degrees of freedom.

Ardekani et al. (1999) proposed the use of subspace modelling and maximum likelihood estimation in the detection of fMRI activations. This method identifies both the dimension and the basis vectors of the nuisance subspace (confounds) using an ML estimation method.

The Kolmogorov-Smirnov (KS) statistic is widely used in the analysis of fMRI data, [for a list of publications see Aguirre et al. (1998a)]. The KS-statistic is based on the maximum distance between the cumulative probability distributions of the different conditions. It does not assume that the noise in the fMRI time series follows a Gaussian distribution. However, independence of the samples is assumed. Indeed, experiments indicate that FPRs, yielded by the KS-test, may excess the tabular values (Aguirre et al., 1998a).

4.4 Detection of activations from statistic images

The ultimate goal of fMRI data analysis is often the detection, localization and delineation of activation regions from SIs. The approaches can be roughly divided into two groups: hypothesis-testing-based methods and modelling-based methods. The hypothesis-testing-based methods control FPRs and detect statistically significantly activated regions. In modelling- or estimation-based methods, activation distributions are estimated and voxels are classified by maximizing the a posteriori probabilities.

Spatial smoothness and smoothing

Spatial smoothness, or coherency, i.e. the presence of cross-correlations of voxel time series is an important issue due to the need for multiple comparison correction. One type of smoothness can be modelled by a continuously differentiable spatial autocovariance function (Zarahn et al., 1997). Filtering the data with a Gaussian kernel creates this type of smoothness. The width of the filter kernel is often expressed with the term of full width at half maximum (FWHM). An alternative expression is the standard deviation of the filter, λ. For a Gaussian filter, these

two are related according to formula

$$\lambda = \frac{\mathrm{FWHM}}{\sqrt{8\ln 2}}. \tag{16}$$

Spatial smoothing of data with a Gaussian filter is a debated issue. It is argued that the best smoothing filter is one that matches the objects to be identified (Worsley and Friston, 1995). However, it should be noted that only the detection of objects is considered then. If other aspects, like the localization of the edges of objects, are considered, the issue is more complex. It is generally known that spatial smoothing may dislocate edges and fuse neighboring objects. The second reason for spatial smoothing is that statistical inferences and multiple comparison correction utilizing the theory of Gaussian random fields, implemented as SPM'99 software (Wellcome Department of Cognitive Neurology, London, UK, http://www.fil.ion.ucl.ac.uk/spm/), assume that the data are spatially smooth (Worsley and Friston, 1995). A Gaussian random field is one that has a Gaussian distribution at every point and at every collection of points. To fulfill the smooth Gaussian random field requirement, the fMRI data are smoothed using a Gaussian filter. Several methods for the estimation of the level of smoothness have been developed (Worsley et al., 1992; Kiebel et al., 1999; Forman et al., 1995). Typically, the methods are based on the variance of the gradients in statistic or residual images. In multi-subject analysis, smoothing is used to ensure that effects between subjects are assessed on a reasonable spatial scale with respect to functional anatomy.

Generally, SIs calculated from heavily smoothed data are able to find large areas of weak activation, while SIs calculated from unsmoothed or lightly smoothed data are sensitive to small but strong foci and also to noise. Multifiltering approaches are proposed to find both types of activations. Poline and Mazoyer (1994) proposed a multiscale method in which the (PET) image is filtered successively with Gaussian filters of increasing widths. Skudlarski et al. (1999) studied a modification in which SIs obtained from smoothed data were added to the SI obtained from unsmoothed data. Also this simpler approach was found to be powerful in practice.

Descombes et al. (1998a) replaced the Gaussian filtering with an spatio-temporal edge preserving MRF-based noise reduction in order to avoid blurring and to preserve the resolution of data. Kruggel et al. (1999) compared a finite impulse response temporal low-pass filter, a temporal Gaussian filter, an autoregressive filter, a spatial Gaussian filter and a spatio-temporal MRF-based noise reduction. The best shape recovery and sensitivity were obtained using an MRF filter while the temporal low-pass filter and temporal Gaussian filters provided better linearity. However, the consequences of MRF data restoration to the statistics of the following ordinary voxel-by-voxel data analysis remain unclear. Descombes et al. (1998b) extended the model. A hemodynamic function was estimated for each voxel. A voxel was considered active if the norm of the hemodynamic function was high enough. MRF potentials were used to regularize the activation maps, using potentials between the activation map and parameter maps that characterize the hemodynamic functions.

Hypothesis testing

In the hypothesis-testing-based approaches, it is tested whether the null hypothesis can be rejected with some statistical significance level (called false-positive rate (FPR), α-level of test

or probability of type I error). When a statistical test is applied separately for each voxel, the total number of tests for typical fMRI data is thousands. Hence, the overall probability of finding at least one statistically significant voxel is considerably larger than the level chosen for conducting each individual test. This is called a multiple comparison problem. One method to control overall (family-wise) FPRs is Bonferroni correction. Specifically, to do k tests, one for each voxel, the overall α-level is divided by k to obtain the required voxel-level α-level. The drawback of the Bonferroni correction is that the smoothness of the data may lead to the too conservative thresholds.

Different procedures are different in sensitivity, localization power and delineation accuracy. Omnibus tests (Friston et al., 1991) have no localization power at all. If an omnibus test rejects the null hypothesis, no information about the location of activations is obtained. The procedure is said to control the overall FPR in the weak sense (Friston et al., 1996a). For example, a test that is based on the total number of voxels above some threshold is an omnibus test. High localization power and strong control is obtained by making statistical inferences for each voxel separately. Then, the voxels above some intensity threshold are considered activated. A procedure is said to control the FPR in the strong sense if the probability of a false positive over any set of voxels for which the null hypothesis is true is less than α regardless of the truth of the null hypothesis elsewhere.

Various post-processing operations can be used after the thresholding. By using spatial extent thresholds, the intensity threshold can be lowered, still maintaining a low overall FPR (Friston et al., 1994b). Simple median filtering can be used to eliminate spurious small activations. In a modification called neighborhood filtering (Skudlarski et al., 1999), only the voxels that have a sufficient number of activated neighbors are left to the activation map. However, Skudlarski et al. found that spatial smoothing of images is more efficient than extent thresholding or neighborhood filtering of the SI. Kleinschmidt et al. (1995) heuristically combined spatial information to the correlation coefficient analysis. The spatial extent of activations was delineated by adding neighboring pixels with lower correlation coefficient values.

The approaches to control FPRs and to make multiple comparison correction can be divided into theoretical parametric approaches, non-parametric approaches and simulation-based approaches (Petersson, 1998).

Theoretical parametric approaches. Theoretical parametric approaches are based on Gaussian field approximation. To hold the assumptions, the fMRI data are smoothed before the analysis. Used approximations are only asymptotically true, in the limit of high thresholds. The results exist for voxel-level, cluster-level and set-level inferences. A basic voxel-level test gives the probability that the observed voxel value, or a higher one, could have occurred by chance in the data volume. This probability is commonly called a corrected p-value of the test. Cluster-level tests give a probability that a connected activation region observed could have occurred by chance (Worsley et al., 1992; Poline et al., 1997). Friston et al. (1996a) introduced an analysis to make set-level inferences, i.e. to calculate the probability of getting the observed number of clusters, or more, in the volume analyzed. Together the voxel-level, cluster-level and set-level inferences form a hierarchy of tests that have different regional specificity and power.

Non-parametric approaches. The permutation test theory can be used to detect activations and to handle multiple comparison problem (Holmes et al., 1996; Belmonte and Yurgelun-Todd, 2001; Nichols and Holmes, 2002). An advantage of the randomization or permutation

tests is that few assumptions about the data are needed, because the distributions are constructed from the data itself. The basic idea is to randomly, or by permutation, re-order the acquired scans. SIs are computed for each re-ordering. Summarizing each SI by its maximum value gives the permutation distribution for maximum values. Voxels or regions can be classified as significantly activated or non-activated by comparing actual statistics to the permutation distribution. When permutation tests are used with fMRI, the temporal autocorrelations should be taken into account (Bullmore et al., 1996a; Locascio et al., 1997).

Simulation approaches. Simulations can be used to estimate the significance of data in problems that are otherwise intractable. Naturally also the usual voxel-level, cluster-level and set-level inferences can be based on the simulations. Simulation approaches are dependent on adequate characterization and modelling of image noise. The number of simulations must be sufficiently high to determine the tails of probability distributions with high precision. Forman et al. (1995) estimated the probability of different cluster sizes with simulated SIs. The images were filtered with Gaussian filters of different widths and thresholded with different thresholds. Thereafter, the occurrence of clusters of different sizes was counted. Poline and Mazoyer (1994) used Monte Carlo simulations to evaluate a multi-scale detection method. Ledberg et al. (1998) estimated the autocorrelation of PET data. This estimate was used to generate simulated images and, in addition, a distribution of cluster sizes was derived. The distribution was used to estimate the probabilities of the clusters of different sizes.

Modelling- or MRF-based approaches

Everitt and Bullmore (1999) presented an SI classification method based on mixture modelling. In their approach, it is assumed that the distribution of SI values is a mixture of two distributions, one being the distribution of non-activated voxels and the other being the distribution of activated voxels. It is assumed that every voxel in the SI is drawn either from the specified null distribution f_0 or from the alternative (activation) distribution $f_1(\mu)$, where μ is the mean of the alternative distribution, or in a general case some other unknown parameter or a vector of unknown parameters. Then the mixture density can be written as

$$f(x; \mu, p) = pf_0(x) + (1 - p)f_1(x; \mu), \tag{17}$$

where p is the proportion of non-activated voxels. The p and μ were estimated from the data by maximizing the log-likelihood $\sum_{i=1}^{N} \log f(x_i; \mu, p)$ of the data, where i indexes the N voxels of the SI. After the parameter estimation the a posteriori probability that a voxel is activated was calculated using the Bayes' formula. Standard errors of the parameters were also be estimated. The basic assumption was that all activated voxels follow the same activation distribution whose shape is defined a priori. An additional concern is the stability, or robustness, of the approach. If the number of activated voxels is very small, the estimation of μ or p in a robust way may be difficult.

Hartvig and Jensen (2000) extended the model of Everitt and Bullmore (1999) by also considering the local spatial properties of the data. The SI values from the neighborhood were used to calculate the a posteriori probability that a voxel is activated. Spatial models of different complexity were considered. The models were chosen so that they model the fact that activated areas tend to constitute a group of at least a few voxels but posterior probabilities can be presented in a simple closed form, which is computationally very efficient.

The concerns presented above also apply to this approach. In addition, it is unlikely that any of the presented spatial models represents accurately the true world. However, the authors found that the spatial models improved the estimation of the activation pattern significantly, compared to the nonspatial model of Everitt and Bullmore (1999) and to the smoothing of the data. This demonstrates that even if the spatial model is not accurate or correct, the use of spatial information may improve the classification. However, the accuracy of estimated quantitative values for activation a posteriori probabilities seems to be questionable.

Holmes and Ford (1993) utilized the Markov random fields in the detection of PET activations. In the approach, 2-D SIs were modelled using MRFs with distance-weighted pair-wise interactions, i.e. doubletons. The means of positive and negative activation classes were set to $\pm 2T$, where T was a Bonferroni-corrected threshold. MMP estimation was carried out using the Gibbs sampler with about 1000 successive realizations after a burn-in of 10 iterations. The method was found to be less powerful than simple thresholding with thresholds $\pm T$. The interpretation of the results is difficult. The method cannot be seen as a modelling-based technique giving MMP estimates because neither the activation class nor the MRF model parameters were estimated from the data or otherwise specified in a realistic way. On the other hand, the method was neither treated as a hypothesis testing technique. That is, the parameters were not set so that a pre-determined FPR could be achieved. This is one explanation for the lower power compared to the thresholding technique. Another possible reason was the strong spatial autocorrelation structure of PET data. A possible reason for not tuning the parameters to control FPRs was the large number of simulations that would have been required. As the Gibbs sampler is slow, e.g. compared to the ICM-algorithm, the computational requirements would have been substantial. Another potential problem of the approach, from the viewpoint of hypothesis testing, lies in locality properties. As hundreds or thousands of iterations are carried out it is not clear what effects a deviating distribution at one location might have at distant locations.

Recently, Rajapakse and Piyaratna (2001) segmented SIs into activated and non-activated regions using a Markov random field model. Their model consisted of singleton and doubleton cliques. The distributions of activated and non-activated voxels were assumed to be Gaussian. The mean and standard deviation of the distributions as well as the singleton and doubleton parameters were estimated iteratively from the data after k-means-based initialization. Energy minimization was done using simulated annealing leading to an MAP estimate of the segmentation. Visually inspecting, the activation patterns obtained using the MRF approach were less noisy than those obtained by simple thresholding or spatial extent thresholding. A strong point of the method is that it is data-driven requiring no user-specified parameters. However, an assumption was made that all the activated voxels follow the same Gaussian distribution. No technique to control FPRs was presented.

Genovese (2000) modelled fMRI data using Bayesian procedures. Prior knowledge about the signal was utilized, for example distribution of the lag between the beginning of a task and a hemodynamic response was specified by using earlier data. Markov chain Monte Carlo sampling techniques were used to estimate the posterior distributions of parameters of interest. Activation maps can be created by locating the pixels in which the posterior probability of the stimulus effect being positive is high enough. However, perhaps the main strength of the Bayesian modelling techniques is that they can be used to solve many other problems than

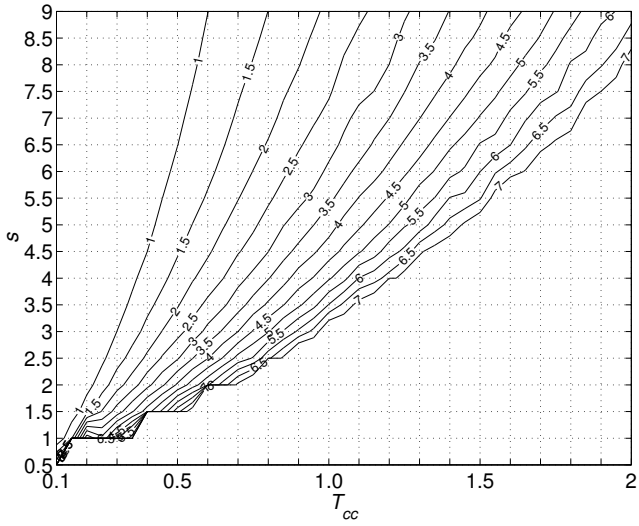

Fig. 5: *False-positive rates (FPRs) at voxel level for contextual clustering as a function of T_{cc} and s. Labels on the curves are $-logP$ values, where P is the FPR at voxel level. The step-wise behavior of the contours in the lower left corner is due to the limited grid spacing and a contour plotting algorithm. Source: Publication III.*

the activation localization. The Bayesian models also give measures to the uncertainty in the estimates. Markov chain Monte Carlo sampling is a computationally demanding operation, which was mentioned as a weakness of the approach. Spatial information was not used in the presented experiments.

4.5 Approach used in this thesis

In this thesis (Publications I–III), SIs were segmented into non-activated and activated regions using the contextual clustering algorithm presented in section 3. Detailed derivation of the algorithm is presented in Publication I. A short summary of the results of Publications I–III is given in this subsection. Different notations in Publications I–III are worth noting. In Publications I and II, the SIs are computed so that activated regions have a negative mean. In Publication III, they have a positive mean. Therefore, the actual classification formulas differ slightly. In this section, the notation of Publication III is used. In all the Publications, the SIs are transformed to z-maps, in which the values of non-activated voxels are assumed to follow the standard normal distribution. As a summary, classification is initialized using Eq. (8) and re-classification is made iteratively using Eq. (9). The number of neighboring voxels is $N_n = 26$, because a 26-connected 3-D neighborhood is used. In the equations, ω_0 represents the background (non-activated voxels) class while ω_1 represents the activation class. Parameter β is the weight of neighborhood information, also expressed as $\beta = T_{cc}^2/s$, where s and T_{cc} are user-specified parameters.

Materials

The contextual clustering method was evaluated using both simulated and measured fMRI data. Simulated activations in Publication I were spheres of a fixed size with a noncentral spherical

Table 1: *The effect of spatial autocorrelations to overall false-positive rates (FPR). λ is the standard deviation (in voxels) of the 3-D Gaussian filter used to create autocorrelations. Source: Publication I, Table II and Publication II, Table 1.*

T_{cc}	s	Image size (voxels)	FPR (Independent Voxels)	FPR (Correlated Voxels)	λ
0.597	2	16384	0.05	0.05	0.5
1.415	6	16384	0.05	0.05	0.5
1.341	6	65536	0.51	0.55	0.6
1.405	6	65536	0.25	0.28	0.6
1.476	6	65536	0.09	0.11	0.6
1.555	6	65536	0.028	0.032	0.6
1.645	6	65536	0.007	0.008	0.6

hole [Fig. 3(a)]. In Publication II, filled spheres of different sizes were used. In Publication III, a simulation pattern including letters was used [Fig. 7(a)]. In Publications I–II, Gaussian noise generated by computer was used, while in Publication III measured fMRI noise was used. The measured fMRI data were collected using various epoch-type paradigms with a visual checkerboard stimulus (Publication I), an electrical median nerve stimulus (Publication II) and a wrist flexing task (Publication III). In addition, in Publication III some of the fMRI data sets were acquired without any stimulus in order to collect baseline data and to measure overall FPRs. All data acquisition was performed using a 1.5-T Siemens Magnetom Vision scanner at the Department of Radiology, Helsinki University Central Hospital.

Most of the analysis work, including all the simulations, were performed using implemented Matlab (The MathWorks, Inc., Natick, MA) functions. In Publication III, movement correction, smoothing and computation of SIs were performed using the SPM'99 software (Wellcome Department of Cognitive Neurology, London, UK, http://www.fil.ion.ucl.ac.uk/spm/) running on the top of Matlab.

False-positive rates and the effect of spatial autocorrelations

Controlling of false-positive rates (FPRs) is a central problem in the detection of activations from fMRI data. FPRs at voxel level were studied using simulated null z-maps. In Publication I, the studies were restricted mainly to $s = 6$ while in Publication III several values for s were used. From Fig. 5 it can be seen that a voxel-level FPR decreases rapidly as T_{cc} is increased or s is decreased. For instance, $(T_{cc}, s) = (1.0, 5)$ gives an approximate false-positive rate FPR $= 10^{-4}$, $(T_{cc}, s) = (1.3, 5)$ gives FPR $= 10^{-6}$ and $(T_{cc}, s) = (1.0, 3.5)$ gives also FPR $= 10^{-6}$. As a comparison, with the thresholding technique (equivalent to $s \to \infty$), threshold T should be set to a value of $T = 3.7$ to obtain FPR $= 10^{-4}$, and to a value of $T = 4.8$ to obtain FPR $= 10^{-6}$. The drawback of increasing T_{cc} is decreased detection sensitivity, while decreasing s leads to lower segmentation accuracy.

Sensitivity to spatial autocorrelations generated by a Gaussian filter was studied in Publications I–II using simulated data, which were convoluted by a Gaussian kernel. The spatial autocorrelations were found to increase the error rates (FPRs) at voxel level. However, at

Table 2: *Overall and voxel-level false-positive rates (FPRs) obtained using simulations, and Bonferroni-type correction made to overall FPRs. Spatially independent voxels were used. Source: Publication I, Tables I,II and Publication II, Table 1*

T_{cc}	s	Image size	overall FPR	voxel-level FPR	$\frac{\text{overall FPR}}{\text{voxels}}$
0.597	2	16384	0.05	3.1×10^{-6}	3.1×10^{-6}
1.415	6	16384	0.05	3.1×10^{-6}	3.1×10^{-6}
1.341	6	65536	0.51	1.1×10^{-5}	7.8×10^{-6}
1.476	6	65536	0.09	1.5×10^{-6}	1.4×10^{-6}
1.645	6	65536	0.007	9.0×10^{-8}	1.1×10^{-7}

the overall (volume) level the effect was found to be relatively small (see Table 1). An explanation is that while the spatial autocorrelations increase the FPRs at voxel level, also the effective number of resolution elements in the whole volume is decreased. These two phenomena may partially cancel each other. The results from Publications I–II indicate that the simple Bonferroni-type correction seems to approximately relate FPRs between voxel and volume levels (Table 2). The approximation should not be extended outside the parameter values used in Publications I–II. If in doubt, the overall FPRs can be partially validated by simulations as in Publication III. However, it should be noted that Gaussian smoothing is not necessarily adequate to model spatial correlations.

Empirical overall FPRs were studied in Publication III. It was found that the overall FPRs exceeded the expected FPRs, especially when designs with long epochs were used. This was the case with the all tested methods: Bonferroni-corrected intensity thresholding, Gaussian random field based thresholding, optionally combined with spatial extent thresholding, and contextual clustering. The reason is unknown. A plausible explanation is spatial coherency that cannot be modelled with a stationary autocorrelation field. That kind of spatial coherency moves the mean of null distribution away from zero (Zarahn et al., 1997). We have found some indications about spatially correlating "spiking"-artifacts from some data sets, which may, at least partially, explain the false positives. Also the motion is a possible explanation. The FPRs were decreased on the average when the estimated realignment parameters were included to the GLM as covariates.

Sensitivity, specificity and segmentation accuracy

Good detection sensitivity is an opposite aim to good specificity, i.e. to a low FPR. Sensitivity vs. specificity measurements can be done only on simulated data as the "true" classification of fMRI cannot be determined. In this work, sensitivity is understood as the proportion of detected activated voxels from all activated voxels. Different approaches to study sensitivity were used in Publications I–III. In Publication I, the decision parameter T_{cc} (called a in Publication I) was varied and the measured true positives were plotted as a function of false positives. In Fig. 6, some results of this ROC study are presented. In Publications II–III, the overall FPR of different methods was fixed. Sensitivity was studied using computer-generated noise (Publication II) and measured fMRI noise (Publication III). Some results from Publication III

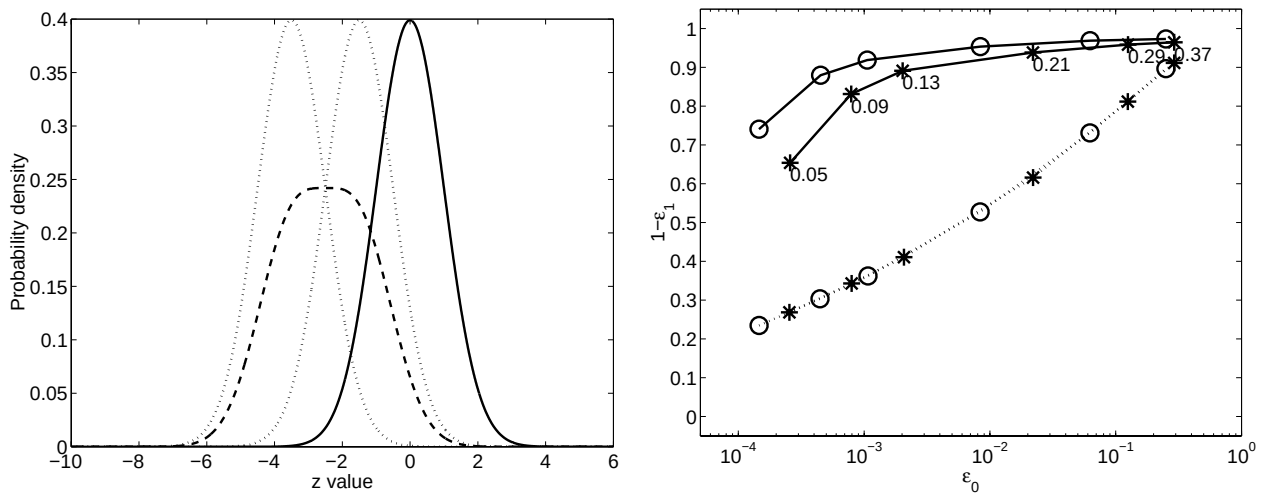

(a) (b)

Fig. 6: *Sensitivity vs. specificity study using a simulated activation pattern [see Fig. 3(a)]. (a) Density functions of background (solid line), two Gaussian activation densities (dotted lines) and the resulting mixed density (non-Gaussian) of activations (dashed line). (b) Receiver operator characteristic (ROC) curves of contextual clustering (solid lines) and thresholding (dotted lines). The ROC curves show the probability of correctly classifying the activation voxels* $(1 - \epsilon_1)$ *on the vertical scale and the probability of misclassifying the background voxels* (ϵ_0) *on the horizontal scale.* $\circ$*: spatially uncorrelated noise;* $*$*: correlated noise. Source and notation: Publication I.*

are illustrated in Fig. 7.

Simulation experiments showed that the sensitivity of contextual clustering is almost universally better than that of voxel-by-voxel thresholding. Compared to the cluster-size thresholding, the situation is more complicated and depends on the actual parameter values and the size and strength of the activation object (Publications II–III). It was also found that when the overall FPR is fixed to the same level among different methods, the voxel-level FPR of cluster-size thresholding is high (Publication II). Contextual clustering had only a slightly higher voxel-level FPR than voxel-by-voxel thresholding. When a cluster-size threshold is used, a false activation region always consists of at least the number of voxels specified by the spatial extent threshold.

If the probability of misclassifying non-activated voxels near a true activation is the same or almost the same as the probability at distant locations, we define that the method has a good segmentation (delineation) accuracy. Effect of contextual information to the segmentation accuracy was studied in Publications II–III. As expected, voxel-by-voxel thresholding without spatial smoothing or contextual information is the most specific method in the neighboring voxels of activated regions. Spatial smoothing substantially decreased segmentation accuracy (Publication III). Performance of thresholding, cluster-size thresholding and contextual clustering can be visually assessed from Figs. 7 and 8. Parameter β defines the weight for contextual information. In most experiments, β was chosen using $\beta = T_{cc}^2/s$. If the value of weight parameter s is chosen to be sufficiently large, e.g. $s = 6$, a relatively good segmentation accuracy is achieved and possible filling effects are avoided. In addition, Eq. (9) has only one root for

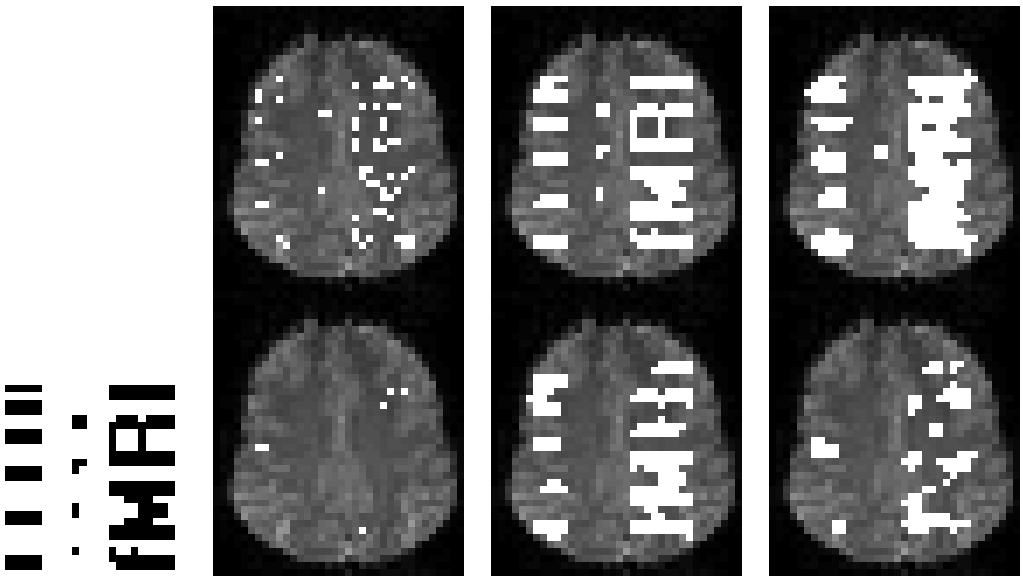

(a) (b) (c) (d)

Fig. 7: *Detection and delineation of a simulation phantom (2.5% signal rise) added to measured fMRI baseline images. Analysis was based on 120 and 60 scans in the upper and lower row, respectively. (a) Simulation phantom, (b) detection using voxel-by-voxel thresholding, (c) contextual clustering, (d) spatial smoothing and voxel-by-voxel thresholding followed by cluster-size thresholding. Source: Publication III.*

T_{cc}, when β is chosen according to $\beta = T_{cc}^2/s$. This seems to reduce the possibility that the classification of a voxel could change from non-activated to activated when parameter T_{cc} is increased. By decreasing s the segmentation accuracy was decreased but sensitivity increased (Fig. 8 and Publications II–III). Hence, s can be seen as a parameter that allows adjusting the tradeoff between sensitivity and segmentation accuracy. Finally, it should be noted that as $s \to \infty$, the weight of contextual information $\beta \to 0$, and the behavior of the clustering algorithm approaches the voxel-by-voxel thresholding.

The contextual clustering method is capable of detecting small activations. Capability to detect small activations was noticed, e.g. in the simulation experiments of Publication II. As a conclusion, at least with some parameter settings, the contextual clustering algorithm can detect activations of only one voxel in size almost as well as voxel-by-voxel thresholding (with a fixed overall FPR). For larger activations, the contextual clustering algorithm is more sensitive. It is worth noting that cluster-size thresholding cannot detect activated areas smaller than the cluster-size threshold - unless spatial smoothing has spread the activation cluster or neighboring voxels exceed the intensity threshold by chance.

Reproducibility

The reproducibility study is an evaluation method that can be used even when the ground truth is unknown (Baumgartner et al., 1997; Casey et al., 1998). Reproducibility of the results depends on multiple factors beginning from the reproducibility of the hemodynamic response.

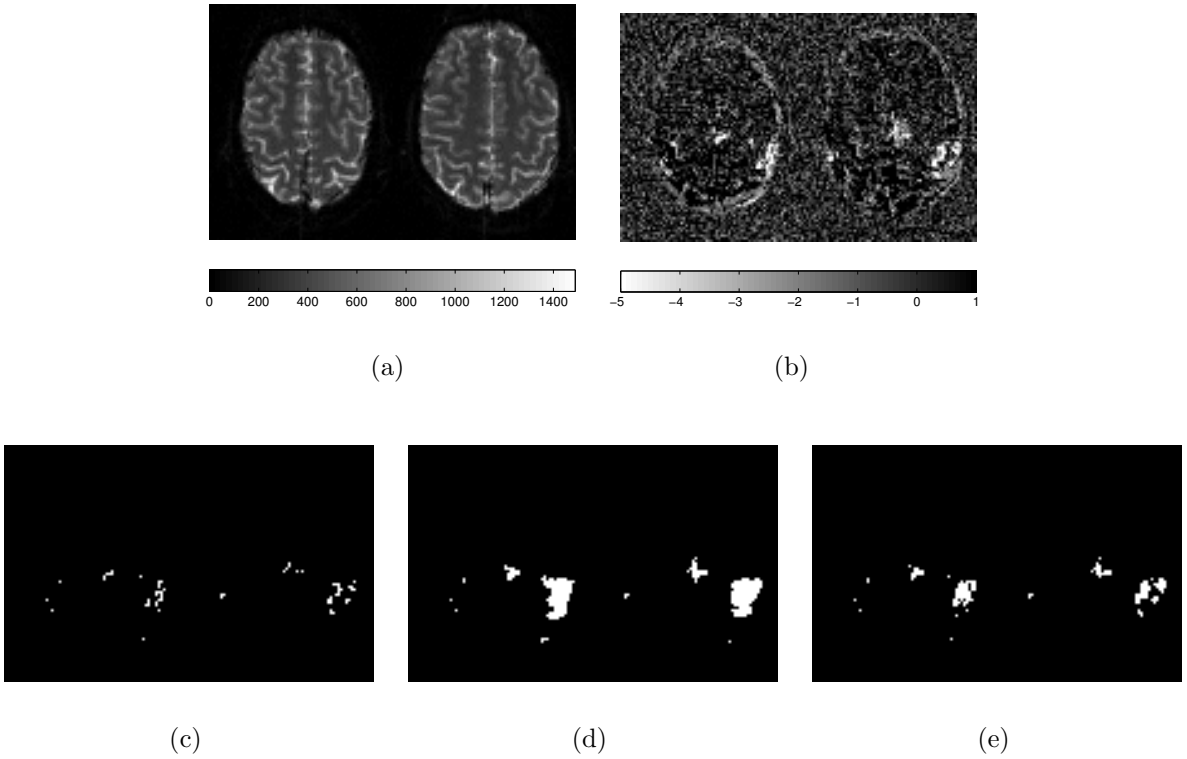

Fig. 8: *Localization of fMRI activations in two subsequent slices. (a) The EPI slices. (b) The corresponding SIs (z-maps). Responses to stimulation of the right median nerve in the contra- and ipsilateral SMI and SMA can be seen as brighter areas. In the SMI, activation is seen in two adjacent sulci (precentral and postcentral). Segmentation of the SI by (c) voxel-by-voxel thresholding, (d) contextual clustering with* $s = 2$ *and (e) with* $s = 6$*. The estimated overall FPR is* 0.05*. Source: Publication II.*

The motivation behind reproducibility studies conducted in this thesis was the assumption that non-reproducible noise may have a different effect on different analysis strategies.

Reproducibility of the activation patterns was studied in Publication III (see Fig. 9). It was found that contextual clustering improved reproducibility, as compared to the voxel-by-voxel thresholding. By using spatial smoothing, it was possible to obtain similar improvement in reproducibility but with lower segmentation accuracy. In a related study (Salli et al., 2001) using the same material as in Publication III it was found that the highest reproducibility was obtained with $s = 2$, but values $s = 6$ and $s = 10$ gave almost equally high reproducibility. However, too detailed conclusions should be avoided as the material only consisted of four sessions on one volunteer.

Computational efficiency

One of the goals of this work was to develop an activation localization algorithm which is computationally efficient enough to be used in clinical practice, or even to be used to monitor on-line the progress of imaging. On a typical PC, it takes only a few seconds to cluster one 3-D image using a Matlab script (Publication I). By using an optimized code (e.g. C-function) or a computer with parallel architecture the execution time could likely be reduced significantly.

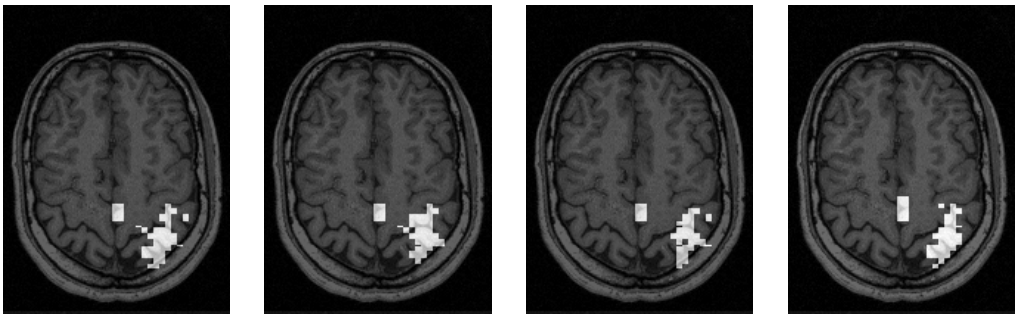

Fig. 9: *An fMRI experiment consisting of a simple motor task was performed four times on the same subject. SIs were computed using a GLM and activations were segmented with the contextual clustering algorithm* $(T_{cc}, s) = (1.44, 6)$*. The upper left image of Fig. 6b of Publication III was computed using the four activation maps shown here.*

Permutation approach

So far we have assumed that SIs are computed using parametric statistic, and FPRs are estimated using simulated data. It will be outlined below how permutation tests could be used with the contextual clustering algorithm. Further analysis and validation of the approach will be left for future work. An advantage of the permutation testing approach is that normality of the fMRI time series is not assumed. In addition, the multiple comparison problem can be solved. As an output the described permutation procedure will give p-values for each activation region detected by the contextual clustering algorithm.

According to Eq. (9), the last step (of the last cycle) of the contextual clustering consists of thresholding the map $z' = z + \frac{\beta}{T_{cc}}(u - 13)$ by T_{cc}. The z'-map can be understood as an activation-enhanced version of the original z-map. Thresholding of z' by T_{cc} gives the result of contextual clustering. Hence, the permutation methodology developed for the assessing of the significance of activations [e.g. Holmes et al. (1996); Nichols and Holmes (2002)] can be directly utilized.

In principle, any statistic can be used to compute SIs, and the results of permutation tests are still valid. However, for reasons of optimality and predictability, we recommend that the SIs are computed using t-statistic. Especially, the contextual enhancement will fail if the mean of non-activated areas is non-zero. It is also assumed that the values in time series are temporally uncorrelated. It seems that correlations can be essentially reduced by high-pass filtering and pre-whitening the time series (Woolrich et al., 2001).

In order to give p-values to the activated regions, a suitable test statistic, which differentiates the detected regions, needs to be defined. We propose here the sum of z values over the activation region, although other measures, like the size of activation, can be used, too. Multiple comparison correction can be made by considering a maximal statistic (Nichols and Holmes, 2002) that is the maximum of the calculated sum values in this case. A large number (preferably at least 1000) of z-maps are computed using random orderings of the scans. For each ordering, a z'-map is computed and contextually clustered. The sum of z'-values is computed for every activation region and the maximum of the sum values is stored. Together the maximum values from all the random orderings and the actual ordering form an empirical distribution for the

maximal statistic. The multiple comparison corrected p-value for each detected activation region is the proportion of the permutation distribution for the maximal statistic that is greater than or equal to the sum of z'-values obtained using the actual ordering.

Parameters T_{cc} and β must be chosen properly to enhance the activation regions. If too large T_{cc} is chosen, the activation regions are not enhanced. Similarly, if T_{cc} is chosen to be too small, almost all voxels are enhanced, resulting in no actual enhancement for activation regions. In both cases the results are still statistically valid but it is unlikely that any activations are detected. The problem here is that T_{cc} and β need to be chosen before the analysis is performed. If the t-statistic is used to compute the SIs, the results from the Publications I and III can be used to set the parameters so that only a small proportion of the voxels is initially classified as activated. Thereafter, the results from the permutation testing can be used to reject the activation regions whose p-value is larger than 0.05, for example.

4.6 Testing or modelling activations?

As already discussed, the two fundamentally different ways to classify voxels of fMRI statistic images into activated and non-activated voxels are

1) by controlling the FPRs (either voxel-level or overall), and

2) by finding a posteriori the most probable segmentation, or by minimizing the total number of false classifications - both false positives and false negatives. A variation of this approach would be to minimize the weighted sum of false positives and negatives.

Naturally the goals are loosely defined because the concept "activation" cannot be defined easily. Traditionally, mostly way 1) has been used in the fMRI activation detection while type 2) classification is widely used i.e. in the brain tissue classification. In this thesis, the way 1) has been adopted. The primary reason is that the way 1) requires information only about the distribution of non-activated voxels while the way 2) requires the modelling of the activation distributions.

Potentially, the modelling of activation distributions could provide a posteriori probabilities for a voxel being activated or non-activated voxel. However, the modelling of fMRI activation distributions seems to be a much more complicated issue than e.g. the modelling of different tissue classes in the segmentation of structural brain MR images. In general, any parametric forms (e.g. Gaussian or Poisson) for intensity distributions of activations in SIs can hardly be realistic. It is well possible that fMRI data consist of multiple activation spots. Each of the spots may have its own distribution. In addition, the distribution of statistic values most likely vary spatially within each activation spot. Realistic modelling of all these factors would be important but difficult, considering that the proportion of activated voxels may be very small.

In approach 1) only the distribution of non-activated voxels is required. This information is provided by the definition of the used statistic. Voxels whose statistic value is high enough to occur by chance are considered activated. In this section and in Publications I–III it was demonstrated that spatial context can be used to decrease the effect of random noise and to increase the probability of detecting weak activations. In addition, the shapes of activations could be reconstructed relatively accurately in the simulation experiments.

5 Multimodal imaging

Different imaging modalities provide complementary information. The combination of data acquired using different methods is useful but not straightforward. In this section, some case studies about combining and comparing structural and functional brain imaging or measurement data are presented. Especially, methods for segmentation, registration, visualization and comparison of fMRI and MEG localization results are discussed.

5.1 Registration

A basic requirement for multimodal imaging is the registration of different image modalities. The co-registration between MEG and MRI is not straightforward because MEG does not provide any anatomic landmarks. In Publications IV–V, a standard procedure based on the anatomical landmarks (preauricular points and the nasion) was used. These, as well as three head position indicator coils attached to the skin, were located with a three-dimensional digitizer (Polhemus, Inc., Colchester, VT, USA). The head position within the measurement dewar was determined using current fed into the indicator coils (Ahlfors and Ilmoniemi, 1989). Co-registration between MEG and MRI was determined by locating the preauricular points and nasion from the MR images. The transformation between structural high-resolution MRI and fMRI activation maps (Publications III–V) was implemented by utilizing slice-positioning information included into the header files of structural high-resolution MR and functional echo-planar images. In this approach, it is assumed that the subject has not moved between the structural MRI and fMRI sessions. It is also assumed that geometrical distortions are not significantly different between the fMRI and MRI data sets. This is an issue that should be studied in the future and, if necessary, a distortion correction method may be used. The registration algorithm used for the MRI and SPECT data (Publication VI) follows a noniterative least-squares method using a singular value decomposition of a 3×3 covariance matrix (Arun et al., 1987). The used approach is based on external skin markers or anatomical markers defined interactively on the screen using a mouse. After the registration the data sets are in the same coordinate system and thus comparable.

5.2 Comparing and combining fMRI and MEG

Although MEG is sensitive to millisecond-scale changes in mental activity, its ability to resolve source localization is limited by the ill-posed inverse problem. PET and especially fMRI have a higher spatial resolution than MEG but worse temporal resolution. In the context of functional brain imaging, first attempts to restrict the electromagnetic inverse problem with PET data were done by Heinze et al. (1994). However, fMRI provides even better spatial resolution than PET, event-related fMRI techniques providing the possibility to use stimulus setups that are identical to or slightly modified compared to those used in MEG. There have been several studies on the regularization of the MEG inverse problem using the physiological and structural information available from MRI and fMRI [see e.g. George et al. (1995); Liu et al. (1998); Dale et al. (2000) and Publication IV]. The use of structural MRI can be based on the findings that the majority of the magnetic signals observed arise from the gray matter. Additionally, the neurons are preferentially oriented perpendicular to the cortex. This information can be used

to constrain the orientation of sources. The usefulness of fMRI arises from the assumption that at many activations, sources contributing to the MEG signal can be detected with fMRI. However, it is possible that areas classified as active by fMRI produce no MEG signal (extra fMRI sources). Conversely, it is possible that some electromagnetically active sources are not detected by fMRI (invisible fMRI sources). Therefore, the MEG solution space should not be overconstrained by fMRI data (Liu et al., 1998). Despite some mismatches, combined fMRI, MRI and MEG data have been successfully used to obtain accurate spatiotemporal maps of human brain activity, including information about statistical reliability and spatial accuracy at different locations (Ahlfors et al., 1999; Dale et al., 2000).

In MEG, a common approach to the inverse problem is the modelling of the activation sources with equivalent current dipoles (ECD). An ECD is the simplest electrical current element that could explain the measured magnetic field. In Publication IV, the fMRI data were used to specify the locations of the ECDs while the time-varying intensity and orientation information was obtained from MEG. Another approach is to define the locations of all possible sources a priori and to determine the components of each dipole. As the number of possible source locations is generally larger than the number of sensors, minimum-norm solutions have been used. Additionally, fMRI data can be used to weight the possible locations of sources. Liu et al. (1998) conducted Monte Carlo simulations, studied the usefulness of the approach and quantified the effects of extra and invisible fMRI sources. Information from the MRI was found to give an improved solution for the MEG inverse problem with high spatial and temporal resolution.

In Publication IV, an eight-dipole model fitted to MEG data was constrained with fMRI data. The MEG data were obtained with the Neuromag-122 magnetometer at the BioMag Laboratory, Helsinki University Central Hospital. The objectives of the study were

- to compare the localizations obtained with MRI and fMRI separately, and
- to study the time course of activation at different cortical sites.

Related to present thesis, image processing tools for the comparison of the locations of fMRI and MEG activations were designed and implemented.

To compare the source locations deduced from fMRI and MEG data, the Euclidean distance between the center points of activations detected by MEG and fMRI was measured. The location of a fitted current dipole was used directly as a center point of activation in MEG. In fMRI, an activation region typically consists of a number of voxels. The centroid (i.e. the center of mass) of an activation area was used to specify the location of the fMRI activation. This required a method to cluster the activated voxels from the fMRI into separate activation areas.

The active voxels of thresholded fMRI statistic images were grouped into 6–8 clusters using the k-means clustering (Bow, 1984). The objective function to be minimized is the sum of squared distances between each voxel and its cluster center:

$$S = \sum_{\forall i} [i - C(i)]^2, \tag{18}$$

where $C(i)$ is the mean of the cluster that voxel i is assigned to. The initialization was done manually.

To achieve the second objective, fMRI information was used as a spatial constraint in the solution of the MEG inverse problem. The position of each dipole was fixed to the centroids of fMRI activation areas. The strength and direction of each dipole were allowed to vary so as to produce a least-squares fit to the measured magnetic field pattern at each point of time during the entire sweep.

The results of Publication IV demonstrate that the integrated use of MEG and fMRI can provide plausible information about brain function after somatosensory stimulation, with high resolution in both spatial and temporal domains.

5.3 Segmentation and multimodal visualization

Structural MRI data can be used to create presentations about brain surface. In many occasions, presentations of fMRI and MEG localization results on 3-D reconstruction of cortex are useful. For example, maps of vital areas, such as language, motor function, and memory, can be used for planning of operations on gliomas (Publication V). To produce rendered 3-D multimodal visualization, tools for the analysis of fMRI and MEG data, segmentation of MRI data, registration and transformation of fMRI, MEG and MRI data to common coordinates system and multimodal visualization techniques are needed.

Various segmentation methods for the medical image data exist. In most applications, the methods are not fully automatic or reliable but can greatly reduce the amount of needed human work. For the 3-D visualization of cortex, a brain segmentation (extraction) method is needed. Deformable surfaces and region growing-based algorithms form two widely used groups of methods. When deformable surfaces are used, some initial, or a priori, model of the surface is deformed using actual image data to match the model with the outer edge of brain. The deformable models are especially efficient when the images are noisy and contain incomplete edge information (Lötjönen et al., 1999). A simple region growing-approach is often adequate for the extraction of the brain from high-quality MR images as the contrast between the gray matter and the cerebral spinal fluid is high. In the basic version, a seed voxel is chosen to represent an initialization region. Thereafter, the adjacent voxels whose gray-level differs at most by a specified threshold from the average gray level of the region are merged to the region. This is repeated until no new voxels can be merged.

In this work, the extraction of brain from MR images was based on a region growing algorithm additionally utilizing edge information (Yu et al., 1992; Sipilä et al., 1992). An easy-to-use segmentation software with graphical user interface and interactive correction tools was designed and implemented. The results were validated by visual inspection.

Several ways to visualize combined 3-D structural and functional image data exist. Often the activations are projected onto brain surface. The cortical inflation techniques allow the 3-D visualization of deeply located sources [see e.g. Fischl et al. (1999)]. Spatiotemporal evolving of brain activity can be presented as a movie (Liu et al., 1998).

Rendering and shading methods are needed to create projection images from 3-D data. Rendering and shading algorithms use either the original (possibly segmented) voxel data or calculated surface (usually triangulated) presentation of the objects of interest. In this thesis, two relatively fast volume-rendering methods, operating directly on the volume data, were used to perform renderings. The first method utilizes a prebuffer technique (Ylä-Jääski et al., 1991) to speed up the rendering. The prebuffer is an intermediate image plane parallel to the object

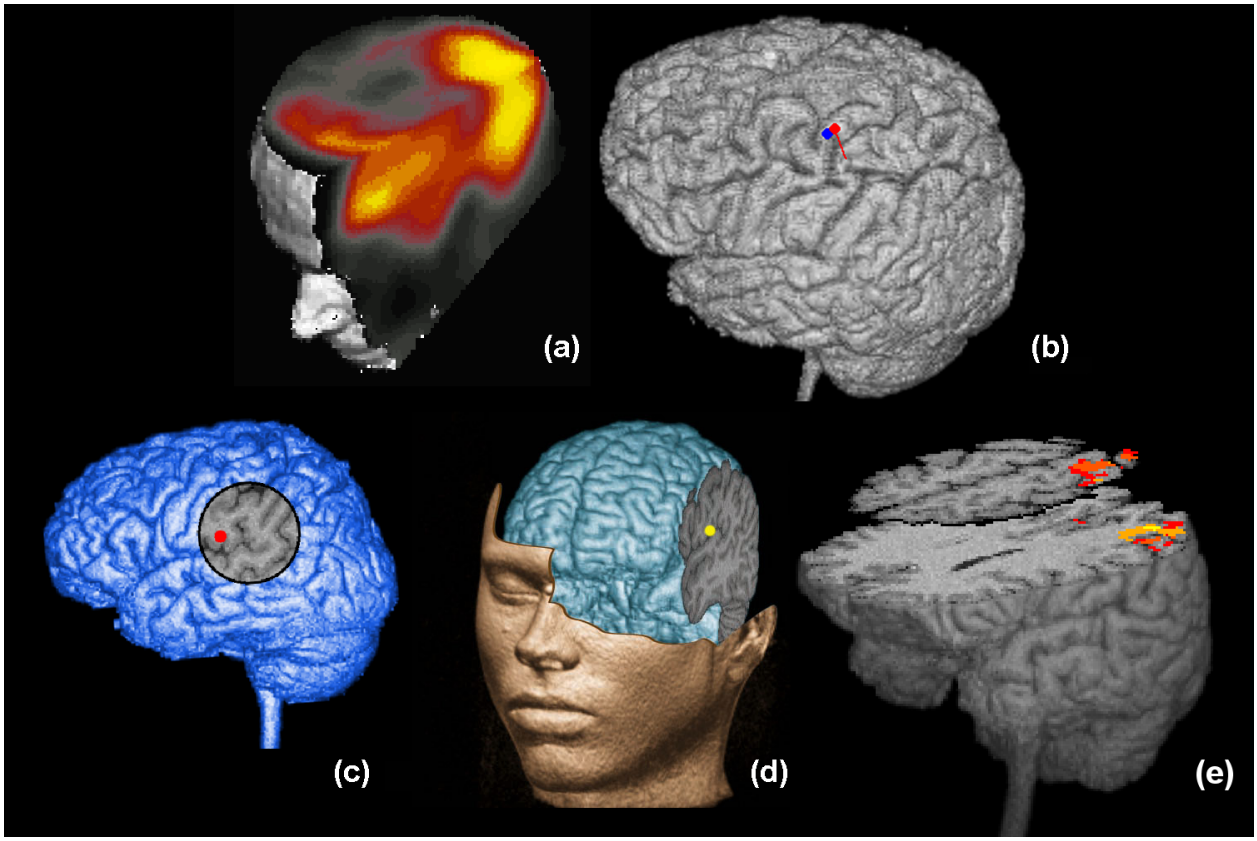

Fig. 10: *Examples of 3-D multimodal visualizations. (a) Surface-shaded image constructed using MRI combined with SPECT data on a cut plane in a man with a cerebral infarct (Publication VI). (b) The location of an MEG current dipole source representing an evoked response for electric stimulation of the right median nerve (red dipole) and the center of activation shown by fMRI (blue dot) (Publication V). The MEG localizations in (c) and (d) were obtained by recording the neuromagnetic field in response to an auditory stimulus and by determining the location of a current dipole source. In (c) the original MRI data at the depth of an MEG response are shown using gray values inside a circle. The center of the circle indicates the localization result at the opposite side of the brain in order to visualize cerebral asymmetry. Source: Tiihonen et al. (1998). In (d) a cut plane is used to visualize an MEG localization result. Published e.g. in Kaplan-Solms and Solms (2000). In (e) fMRI activations detected using contextual clustering [$T_{cc} = 1.3$ (red), $T_{cc} = 1.7$, $T_{cc} = 2.1$, $T_{cc} = 2.5$ and $T_{cc} = 2.9$ (yellow) ($s = 6$ in all cases)] are visualized on two slice levels.*

slices. This technique was used with a gradient shading method based on the surface normal vectors estimated from a calculated distance map. This approach was used in Publication VI and Fig. 10(a) of this overview. The second method uses the Stanford VolPack volume renderer (Lacroute and Levoy, 1994). The Stanford VolPack renderer uses a similar prebuffer technique as the first method but also includes additional optimization techniques based on pre-computed data structures. The shading model of the VolPack is based on the surface orientation estimated from the original 3-D data. Also the partial transparency of the voxels is modelled. This shading approach was found to give cortex renderings of good quality [Fig. 10(b)-(e)]. In addition to the used pre-buffer techniques, several other volume rendering acceleration techniques exist, e.g. the use of "probe" rays (Pyökkimies et al., 2001) can speed-up rendering.

In a neurosurgery application, MRI, fMRI and MEG data are fused for planning of operations on gliomas, for example. A "brain map" combining the information from these modalities is produced for a neurosurgeon, aiding the identification of important functional areas of the brain during the operation. The map consists of surface-shaded 3-D brain images, constructed from the anatomical MRI. The MEG and/or fMRI localization results are visualized on the brain surface. On the other hand, combined MRI and SPECT studies may be useful in the diagnosis of many diseases (Publication VI). Various multimodal 3-D visualization modes are shown and explained in Fig. 10. While the clinical value of 3-D renderings has been somewhat unclear so far, they will most likely have an important role e.g. in surgery (Shahidi et al., 1998). In addition, 3-D renderings have proven to be useful in visualizing research results e.g. in scientific journals.

6 Concluding remarks

Aspects related to the analysis of fMRI data and multimodal brain imaging were presented and discussed in this work. Especially, a new fMRI activation detection and delineation method utilizing spatial neighborhood information was developed and studied. It was shown how weak and therefore statistically insignificant activations changed to significant when spatial information was used. This was achieved without using models for the distribution of activated voxels or estimating any segmentation parameters.

Many interesting topics were restricted outside this thesis. These include the usefulness of more complicated potential functions or larger neighborhoods or utilization of anatomical or topological information. An interesting possibility would be to confine the analysis to the cortex and to use a surface-based coordinate system [e.g. Fischl et al. (1999); Andrade et al. (2001)]. Problems specific to multi-subject studies were not discussed either.

A question not addressed is how stimulus-related activation should be defined. Any stimulus will cause changes in the neural activity (and hemodynamic response) at different locations of the brain and potentially in very large areas. As the sensitivity of imaging and analysis methods improve, the volume of statistically significantly activated regions will likely grow. Therefore, the activation voxels and/or regions detected must be classified to more and less relevant. Commonly this is done by assigning statistical significance values to the voxels and clusters. Another approach would be to use, for example, an estimated magnitude of a hemodynamic response.

The ultimate goal of data analysis should be kept in mind. For example, a neurosurgeon might be interested in the most likely location of primary motor cortex, or in the list of possible locations. Both are different problems than the detection and delineation of statistically significant activation areas. More research is needed so the that the optimal data analysis procedures can be found out.

A possible strength of fMRI compared to MEG is the fMRI's capability to separate activation regions which are located close to each other. This separation information may be beneficial when used as prior information in the MEG inverse problem. In this context, it is important to avoid data smoothing, which may fuse the activated regions together. Hence, the fMRI activation detection method developed in this thesis may also be useful when fMRI and MEG information are combined.

7 Summary of publications

I Contextual clustering for analysis of functional MRI data (IEEE Trans. Med. Imaging 20:403–414, 2001).

A contextual clustering algorithm was derived and its relation to the Markov random fields, ICM algorithm and hypothesis testing was explained. By using receiver operator characteristics (ROC) analysis, voxel-level sensitivity and specificity of the contextual clustering was studied. Computer-generated noise with and without spatial correlations was used in the ROC analyses. The behavior of the algorithm in the case of multiple activation regions following different distributions was also studied. Voxel-level and overall false-positive rates were estimated and tabulated using simulated, optionally filtered, data. A real fMRI experiment using a visual stimulus was carried out. The contextual clustering algorithm was compared to intensity thresholding.

II Statistical segmentation of fMRI activations using contextual clustering (Proc. of the 2nd International conference on Medical Image Computing and Computer Assisted Intervention (MICCAI'99). Lect. Notes Comput. Sci. 1679:481–488, 1999).

Contextual clustering, intensity thresholding and spatial extent thresholding techniques were compared. Segmentation accuracy, i.e. the false-positive rate in the immediate neighborhood of a strong activation, was studied using simulated data. Sensitivity was tested using activations of different sizes and intensities. Robustness against spatial correlations in the noise term was studied. An fMRI experiment with electrical median nerve stimulation was used as a real data example to illustrate the performance of the various methods. The different techniques were compared by using a fixed overall false-positive rate.

III Reproducibility of fMRI: Effect of the use of contextual information (NeuroImage 13:459–471, 2001).

A typical fMRI study was repeated four times with the same volunteer. Statistic images were computed and the images were segmented into activated and non-activated regions. Thereafter, the locations of the activated voxels were compared by computing reliability maps. Sensitivity and segmentation accuracy of different activation detection approaches were studied using a simulated activation pattern but measured noise. False-positive rates were measured by analyzing measured control state data with various design matrices. The statistic image segmentation methods used in this publication were: Bonferroni-corrected thresholding, contextual clustering using parameters determined by simulations, intensity thresholding using thresholds determined by the Gaussian random field theory and intensity thresholding followed by spatial extent thresholding using intensity thresholds determined by the Gaussian random field theory. Spatial smoothing of the data was used in the last two strategies while unsmoothed data were used with the Bonferroni-corrected thresholding and contextual clustering. Excluding the smoothing, the preprocessing and generation of the statistic images were done in the same way in all cases.

IV Activation of multiple cortical areas in response to somatosensory stimulation: Combined magnetoencephalographic and functional magnetic resonance imaging (Hum. Brain Mapp. 8:13–27, 1999).

Information from fMRI and MEG was combined. Methodology to compare the localization results of fMRI and MEG was developed. The activation sites from fMRI were used to constrain the solution of the inverse problem of MEG.

V Hospital-wide PACS: multimodal image analysis using ATM network (Computer Assisted Radiology: Proc. of the International Symposium on Computer and Communication Systems for Image Guided Diagnosis and Therapy (CAR'96). 399–404, 1996).

Experiments on implementing a hospital-wide picture archiving and communication system (PACS) were described. Multimodal clinical applications utilizing the PACS network and the developed scientific software were presented. Related to the present thesis, visualization techniques and segmentation software were introduced.

VI Registration and display of brain SPECT and MRI using external markers (Neuroradiology 38:108–114, 1996).

A registration and display system for brain SPECT and MRI was developed. The usefulness of the the multimodal approach was shown with images from patients suffering from different illnesses. From the viewpoint of the present thesis, visualization techniques for multimodal data were introduced.

Errata

Publication I: In Section III.C, "The 3-D noise correlation was created in a similar way, but a $128 \times 128 \times 64$ image was filtered..." should be "The 3-D noise correlation was created in a similar way, but a $128 \times 128 \times 32$ image was filtered..."

Publication IV: In Table I, "SII contralateral N20m" should be "SI contralateral N20m" and "SI contralateral P30m" should be "SI contralateral P35m"

Publication VI: Theoretically three markers are adequate for the registration, if they are not colinear.

Author's contribution

All publications included in this thesis are a result of group effort. Majority of the methodological work concerning the developed contextual clustering algorithm in Publications I–III was carried out by the author of this thesis. Especially, the author developed and implemented the different variations of the contextual clustering algorithm, designed, implemented and performed computer simulations and tests. Additionally in Publication III, the author contributed to the design of fMRI experiments and carried out the data analyses. In Publication IV, the author contributed to the development of the methods and tools needed in the comparison of fMRI and MEG localization results including the transformation of fMRI activation maps to MEG coordinates and determination of fMRI activation centroids. The author was the main

responsible for designing and implementing the scientific segmentation and visualization tools used in Publication V. However, the author did not develop or implement the kernel routines of the volume rendering or region growing algorithms. In Publication VI, the author contributed to the multimodal visualizations, but not to the registration or imaging. Especially, Figures 4, 5 and 7 of Publication VI were created by the author. In addition, the author of this thesis has been the main responsible for creating all 3-D visualizations presented in this overview. Publications I–III were mostly written by the author of this thesis.

References

Acharya, R. and Menon, R. P. (1998). A review of biomedical image segmentation techniques. In Singh, A., Goldgof, D., and Terzopoulos, D., editors, *Deformable Models in Medical Image Analysis*, pages 140–161. IEEE Computer Society Press.

Aguirre, G. K., Zarahn, E., and D'Esposito, M. (1998a). A critique of the use of the Kolmogorov-Smirnov (KS) statistic for the analysis of BOLD fMRI data. *Magn. Reson. Med.*, 39:500–505.

Aguirre, G. K., Zarahn, E., and D'Esposito, M. (1998b). The inferential impact of global signal covariates in functional neuroimaging analyses. *NeuroImage*, 8:302–306.

Ahlfors, S. and Ilmoniemi, R. J. (1989). Magnetometer position indicator for multichannel MEG. In Williamson, S. J., editor, *Advances in Biomagnetism*, pages 698–696. Plenum Press.

Ahlfors, S. P., Simpson, G. V., Dale, A. M., Belliveau, J. W., Liu, A. K., Korvenoja, A., Virtanen, J., Huotilainen, M., Tootell, R. B. H., Aronen, H. J., and Ilmoniemi, R. J. (1999). Spatiotemporal activity of a cortical network for processing visual motion revealed by MEG and fMRI. *J. Neurophysiol.*, 82:2545–2555.

Andrade, A., Kherif, F., Mangin, J. F., Worsley, K. J., Paradis, A. L., Simon, O., Dehaene, S., Le Bihan, D., and Poline, J. B. (2001). Detection of fMRI activation using cortical surface mapping. *Hum. Brain Mapp.*, 12:79–93.

Ardekani, B. A., Kershaw, J., Kashikura, K., and Kanno, I. (1999). Activation detection in functional MRI using subspace modeling and maximum likelihood estimation. *IEEE Trans. Med. Imaging*, 18:101–114.

Arun, K. S., Huang, T. S., and Blostein, S. D. (1987). Least-squares fitting of two 3-D points sets. *IEEE Trans. Pattern Anal. Mach. Intell.*, 9:698–700.

Ashburner, J., Andersson, J. L., and Friston, K. J. (1999). High-dimensional image registration using symmetric priors. *NeuroImage*, 9:619–628.

Bandettini, P. A. (2000). The temporal resolution of functional MRI. In Moonen, C. T. W. and Bandettini, P. A., editors, *Functional MRI*, pages 205–220. Springer.

Bandettini, P. A., Jesmanowicz, A., Van Kylen, J., Birn, R. M., and Hyde, J. S. (1998). Functional MRI of brain activation induced by scanner acoustic noise. *Magn. Reson. Med.*, 39:410–416.

Bandettini, P. A., Jesmanowicz, A., Wong, E. C., and Hyde, J. S. (1993). Processing strategies for time-course data sets in functional MRI of the human brain. *Magn. Reson. Med.*, 30:161–173.

Baumgartner, R., Scarth, G., Teichtmeister, C., Somorjai, R., and Moser, E. (1997). Fuzzy clustering of gradient-echo functional MRI in the human visual cortex. Part I: Reproducibility. *J. Magn. Reson. Imag.*, 7:1094–1101.

Baune, A., Sommer, F. T., Erb, M., Wildgruber, D., Kardatzki, B., Palm, G., and Grodd, W. (1999). Dynamical cluster analysis of cortical fMRI activation. *NeuroImage*, 9:477–489.

Belliveau, J. W., Kennedy, D. N., McKinstry, R. C., Buchbinder, B. R., Weisskoff, R. M., Cohen, M. S., Vevea, J. M., Brady, T. J., and Rosen, B. R. (1991). Functional mapping of the human visual cortex by magnetic resonance imaging. *Science*, 254:716–719.

Belliveau, J. W., Rosen, B. R., Kantor, H. L., Rzedzian, R. R., Kennedy, D. N., McKinstry, R. C., Vevea, J. M., Cohen, M. S., Pykett, I. L., and Brady, T. J. (1990). Functional cerebral imaging by susceptibility-contrast NMR. *Magn. Reson. Med.*, 14:538–546.

Belmonte, M. and Yurgelun-Todd, D. (2001). Permutation testing made practical for functional magnetic resonance image analysis. *IEEE Trans. Med. Imaging*, 20:243–248.

Besag, J. (1974). Spatial interaction and the statistical analysis of lattice systems (with discussion). *J. R. Stat. Soc. Ser. B*, 36:192–236.

Besag, J. (1986). On the statistical analysis of dirty pictures (with discussion). *J. R. Stat. Soc. Ser. B*, 48:259–302.

Biswal, B., DeYoe, E. A., and Hyde, J. S. (1996). Reduction of physiological fluctuations in fMRI using digital filters. *Magn. Res. Med.*, 35:107–113.

Biswal, B., Yetkin, F. Z., Haughton, V. M., and Hyde, J. S. (1995). Functional connectivity in the motor cortex of resting human brain using echo-planar MRI. *Magn. Res. Med.*, 34:537–541.

Bow, S.-T. (1984). *Pattern recognition: Applications to large data-set problems.* New York. Marcel Dekker, Inc.

Boynton, G. M., Engel, S. A., Glover, G. H., and Heeger, D. (1996). Linear systems analysis of functional magnetic resonance imaging in human V1. *J. Neurosci.*, 16:4207–4221.

Buckner, R. L., Bandettini, P. A., O'Craven, K. M., Savoy, R. L., Petersen, S. E., Raichle, M. E., and Rosen, B. R. (1996). Detection of cortical activation during averaged single trials of a cognitive task using functional magnetic resonance imaging. *Proc. Natl. Acad. Sci. U.S.A.*, 93:14878–14883.

Bullmore, E., Brammer, M., Williams, S. C. R., Rabe-Hesketh, S., Janot, N., David, A., Mellers, J., Howard, R., and Sham, P. (1996a). Statistical methods of estimation and inference for functional MR image analysis. *Magn. Reson. Med.*, 35:261–277.

Bullmore, E., Horwitz, B., Honey, G., Brammer, M., Williams, S., and Sharma, T. (2000). How good is good enough in path analysis of fMRI data? *NeuroImage*, 11:289–301.

Bullmore, E. T., Rabe-Hasketh, S., Morris, R. G., Williams, S. C. R., Gregory, L., Gray, J. A., and Brammer, M. J. (1996b). Functional magnetic resonance image analysis of a large-scale neurocognitive network. *NeuroImage*, 4:16–33.

Buonocore, M. H. and Maddock, R. J. (1997). Noise suppression digital filter for functional magnetic resonance imaging based on image reference data. *Magn. Reson. Med.*, 38:456–469.

Burock, M. A. and Dale, A. M. (2000). Estimation and detection of event-related fmri signals with temporally correlated noise: A statistically efficient and unbiased approach. *Hum. Brain Mapp.*, 11:249–260.

Casey, B. J., Cohen, J. D., O'Craven, K., Davidson, R. J., Irwin, W., Nelson, C. A., Noll, D. C., Hu, X., Lowe, M. J., Rosen, B. R., Truwitt, C. L., and Turski, P. A. (1998). Reproducibility of fMRI results across four institutions using a spatial working memory task. *NeuroImage*, 8:249–261.

Christensen, G. E., Joshi, S. C., and Miller, M. I. (1997). Volumetric transformation of brain anatomy. *IEEE Trans. Med. Imaging*, 16:864–877.

Clarke, L. P., Velthuizen, R. P., Camacho, M. A., Heine, J. J., Vaidyanathan, M., Hall, L. O., Thatcher, R. W., and Silbiger, M. L. (1995). MRI segmentation: Methods and applications. *Magn. Reson. Imaging*, 13:343–368.

Cohen, D. (1972). Magnetoencephalography: Detection of the brain's electrical activity with a superconducting magnetometer. *Science*, 175:664–666.

Cohen, J. D., Forman, S. D., Braver, T. S., Casey, B. J., Servan-Screiber, D., and Noll, D. C. (1994). Activation of prefrontal cortex in a nonspatial working memory task with functional MRI. *Hum. Brain Mapp.*, 1:293–304.

Cohen, M. S. (1997). Parametric analysis of fMRI using linear systems methods. *NeuroImage*, 6:93–103.

Constable, R. T., McCarthy, G., Allison, T., Anderson, A. W., and Gore, J. C. (1993). Functional brain imaging at 1.5 T using conventional gradient echo MR imaging techniques. *Magn. Reson. Imaging*, 11:451–459.

Cox, R. W. and Jesmanowicz, A. (1999). Real-time 3D image registration for functional MRI. *Magn. Reson. Med.*, 42:1014–1018.

Dale, A. M. and Buckner, R. L. (1997). Selective averaging of rapidly presented individual trials using fMRI. *Hum. Brain Mapp.*, 5:329–340.

Dale, A. M., Liu, A. K., Fischl, B. R., Buckner, R. L., Belliveau, J. W., Lewine, J. D., and Halgren, E. (2000). Dynamic statistical parametric mapping: combining fMRI and MEG for high-resolution imaging of cortical activity. *Neuron*, 26:55–67.

Dempster, A. P., Laird, N. M., and Rubin, D. B. (1977). Maximum likelihood from incomplete data via the EM algorithm (with discussion). *J. R. Stat. Soc. Ser. B*, 39:1–38.

Descombes, X., Kruggel, F., and von Cramon, D. Y. (1998a). fMRI signal restoration using a spatio-temporal Markov random field preserving transitions. *NeuroImage*, 8:340–349.

Descombes, X., Kruggel, F., and von Cramon, D. Y. (1998b). Spatio-temporal fMRI analysis using Markov random fields. *IEEE Trans. Med. Imaging*, 17:1028–1039.

Descombes, X., Mangin, J.-F., Pechersky, E., and Sigelle, M. (1995). Fine structures preserving Markov model for image processing. In *Proc. of the 9th Scandinavian Conference on Image Analysis - SCIA 95*, pages 349–356.

Dubes, R. C., Jain, A. K., Nadabar, S. G., and Chen, C. C. (1990). MRF model-based algorithms for image segmentation. In *Proc. of the 10th International Conf. on Pattern Recognition*, pages 808–814.

Eddy, W. F., Fitzgerald, M., and Noll, D. C. (1996). Improved image registration by using Fourier interpolation. *Magn. Reson. Med.*, 36:923–931.

Everitt, B. S. and Bullmore, E. T. (1999). Mixture model mapping of the brain activation in functional magnetic resonance images. *Hum. Brain Mapp.*, 7:1–14.

Fischl, B., Sereno, M. I., and Dale, A. M. (1999). Cortical surface-based analysis II: Inflation, flattening, and a surface-based coordinate system. *NeuroImage*, 99:195–207.

Forman, S. D., Cohen, J. D., Fitzgerald, M., Eddy, W. F., Mintun, M. A., and Noll, D. C. (1995). Improved assessment of significant activation in functional magnetic resonance imaging (fMRI): Use of a cluster-size threshold. *Magn. Reson. Med.*, 33:636–647.

Frahm, J., Haase, A., and Matthaei, D. (1986). Rapid NMR imaging of dynamic processes using the FLASH technique. *Magn. Reson. Med.*, 3:321–327.

Friston, K. J., Fletcher, P., Josephs, O., Holmes, A., Rugg, M. D., and Turner, R. (1998). Event-related fMRI: characterizing differential responses. *NeuroImage*, 7:30–40.

Friston, K. J., Frith, C. D., Liddle, P. F., and Frackowiak, R. S. (1991). Comparing functional (PET) images: the assessment of significant change. *J. Cereb. Blood Flow Metab.*, 11:690–699.

Friston, K. J., Holmes, A., Poline, J.-B., Price, C. J., and Frith, C. D. (1996a). Detecting activations in PET and fMRI: levels of inference and power. *NeuroImage*, 4:223–235.

Friston, K. J., Holmes, A. P., Worsley, K. J., Poline, J.-B., Frith, C. D., and Frackowiak, R. S. J. (1995). Statistical parametric maps in functional imaging: a general linear approach. *Hum. Brain Mapp.*, 2:189–210.

Friston, K. J., Jezzard, P., and Turner, R. (1994a). Analysis of functional MRI time-series. *Hum. Brain Mapp.*, 1:153–171.

Friston, K. J., Williams, S., Howard, R., Frackowiak, R. S., and Turner, R. (1996b). Movement-related effects in fMRI time-series. *Magn. Reson. Med.*, 35:346–355.

Friston, K. J., Worsley, K. J., Frackowiak, R. S. J., Mazziotta, J. C., and Evans, A. C. (1994b). Assessing the significance of focal activations using their spatial extent. *Hum. Brain Mapp.*, 1:214–220.

Geman, S. and Geman, D. (1984). Stochastic relaxation, Gibbs distributions, and the Bayesian restoration of images. *IEEE Trans. Pattern Anal. Mach. Intell.*, PAMI-6:721–741.

Genovese, C. R. (2000). A Bayesian time-course model for functional magnetic resonance imaging data (with discussion). *J. Am. Stat. Assoc.*, 95:691–719.

George, J. S., Aine, C. J., Mosher, J. C., Schmidt, D. M., Ranken, D. M., Schlitt, H. A., Wood, C. C., Lewine, J. D., Sanders, J. A., and Belliveau, J. W. (1995). Mapping function in the human brain with magnetoencephalography, anatomical magnetic resonance imaging, and functional magnetic resonance imaging. *J. Clin. Neurophysiol.*, 12:406–431.

Golay, X., Kollias, S., Stoll, G., Meier, D., Valavanis, A., and Boesiger, P. (1998). A new correlation-based fuzzy logic clustering algorithm for fMRI. *Magn. Reson. Med.*, 40:249–260.

Gössl, C., Fahrmeir, L., and Auer, D. P. (2001). Bayesian modeling of the hemodynamic response function in BOLD fMRI. *NeuroImage*, 14:140–148.

Goutte, C., Toft, P., Rostrup, E., Nielsen, F. A., and Hansen, L. K. (1999). On clustering fMRI time series. *NeuroImage*, 9:298–310.

Hämäläinen, M., Hari, R., Ilmoniemi, R., Knuutila, J., and Lounasmaa, O. V. (1993). Magnetoencephalography - theory, instrumentation, and applications to noninvasive studies of the working human brain. *Rev. Mod. Phys.*, 65:413–497.

Hämäläinen, M. and Nenonen, J. (1999). Magnetic source imaging. In *Encyclopedia of Electrical Engineering*, volume 12. Wiley & Sons, New York.

Hartvig, N. V. and Jensen, J. L. (2000). Spatial mixture modeling of fMRI data. *Hum. Brain Mapp.*, 11:233–248.

Heinze, H. J., Mangun, G. R., Burchert, W., Hinrichs, H., Scholz, M., Munte, T. F., Gos, A., Scherg, M., Johannes, S., Hundeshagen, H., Gazzaniga, M. S., and Hillyard, S. A. (1994). Combined spatial and temporal imaging of brain activity during visual selective attention in humans. *Nature*, 372:543–546.

Held, K., Kops, E. R., Krause, B. J., Wells, W. M., III, Kikinis, R., and Müller-Gärtner, H.-W. (1997). Markov random field segmentation of brain MR images. *IEEE Trans. Med. Imaging*, 16:878–886.

Hennig, J., Nauerth, A., and Friedburg, H. (1986). RARE imaging: a fast imaging method for clinical MR. *Magn. Reson. Med.*, 3:823–833.

Holmes, A. and Ford, I. (1993). A Bayesian approach to significance testing for statistic images from PET. In Uemura, K., Lassen, N. A., Jones, T., and Kanno, I., editors, *Quantification of Brain Function. Tracer Kinetics and Image Analysis in Brain PET*, pages 521–531. Excerpta Medica.

Holmes, A. P., Blair, R. C., Watson, J. D., and Ford, I. (1996). Nonparametric analysis of statistic images from functional mapping experiments. *J. Cereb. Blood Flow Metab.*, 16:7–22.

Jenkinson, M. and Smith, S. (2001a). A global optimisation method for robust affine registration of brain images. *Medical Image Analysis*, 5:143–156.

Jenkinson, M. and Smith, S. (2001b). The role of registration in functional magnetic resonance imaging. In Hajnal, J., Hill, D. L. G., and Hawkes, D. J., editors, *Medical Image Registration*, pages 183–198. CRC Press.

Jezzard, P. (2000). Physiological noise: strategies for correction. In Moonen, C. T. W. and Bandettini, P. A., editors, *Functional MRI*, pages 173–181. Springer.

Josephs, O., Turner, R., and Friston, K. (1997). Event-related fMRI. *Hum. Brain Mapp.*, 5:243–248.

Kandel, E. R. and Squire, L. R. (2000). Neuroscience: breaking down scientific barriers to the study of brain and mind. *Science*, 290:1113–1120.

Kaplan-Solms, K. and Solms, M. (2000). *Clinical Studies in Neuro-Psychoanalysis: Introduction to a Depth Neuropsychology.* Karnac Books.

Kennan, R. P. (2000). Gradient echo and spin echo methods for functional MRI. In Moonen, C. T. W. and Bandettini, P. A., editors, *Functional MRI*, pages 127–136. Springer.

Kiebel, S. J., Poline, J.-B., Friston, K. J., Holmes, A. P., and Worsley, K. J. (1999). Robust smoothness estimation in statistical parametric maps using standardized residuals from the general linear model. *NeuroImage*, 10:756–766.

Kim, B., Boes, J. L., Bland, P. H., Chenevert, T. L., and Meyer, C. R. (1999). Motion correction in fMRI via registration of individual slices into an anatomical volume. *Magn. Reson. Med.*, 31:964–972.

Kim, S.-G., Lee, S. P., Goodyear, B., and Silva, A. C. (2000). Spatial resolution of BOLD and other fMRI techniques. In Moonen, C. T. W. and Bandettini, P. A., editors, *Functional MRI*, pages 195–203. Springer.

Kim, T. W. and Paik, C. H. (1998). Unsupervised statistical adaptive segmentation of brain MR images using the MDL principle. In *Proc. of the 20th Annual International Conf. of the IEEE Engineering in Medicine and Biology Society*, volume 20, pages 617–620.

Kirkpatrick, S., Gelatt, C. D., and Vecchi, M. P. (1983). Optimization by simulated annealing. *Science*, 220:671–680.

Kittler, J. and Pairman, D. (1985). Contextual pattern recognition applied to cloud detection and identification. *IEEE Trans. Geosci. Remote Sensing*, GE-23:855–863.

Kleinschmidt, A., Requardt, M., Merboldt, K.-D., and Frahm, J. (1995). On the use of temporal correlation coefficients for magnetic resonance mapping of functional brain activation: individualized thresholds and spatial response delineation. *Int. J. Imag. Syst. Technol.*, 6:238–244.

Kruggel, F., von Cramon, D. Y., and Descombes, X. (1999). Comparison of filtering methods for fMRI datasets. *Magn. Reson. Imaging*, 10:530–543.

Kuppusamy, K., Lin, W., and Haacke, E. M. (1997). Statistical assessment of crosscorrelation and variance methods and the importance of electrocardiogram gating in functional magnetic resonance imaging. *Magn. Reson. Imaging*, 15:169–181.

Kwong, K. K., Belliveau, J. W., Chesler, D., Goldberg, I. E., Weisskoff, R. M., Poncelet, B. P., Kennedy, D. N., Hoppel, B. E., Cohen, M. S., Turner, R., Cheng, H.-M., Brady, T. J., and Rosen, B. R. (1992). Dynamic magnetic resonance imaging of human brain activity during primary sensory stimulation. *Proc. Natl. Acad. Sci. U.S.A.*, 89:5675–5679.

Lacroute, P. and Levoy, M. (1994). Fast volume rendering using a shear-warp factorization of the viewing transformation. In *Proc. SIGGRAPH'94*, pages 451–458, Orlando. Florida.

Lai, S., Glover, G. H., and Haacke, E. M. (2000). Spatial selectivity of BOLD contrast: effects in and around draining veins. In Moonen, C. T. W. and Bandettini, P. A., editors, *Functional MRI*, pages 221–231. Springer.

Lakshmanan, S. and Derin, H. (1989). Simultaneous parameter estimation and segmentation of Gibbs random fields using simulated annealing. *IEEE Trans. Pattern Anal. Mach. Intell.*, 11:799–813.

Lange, N. (2000). Statistical procedures for functional MRI. In Moonen, C. T. W. and Bandettini, P. A., editors, *Functional MRI*, pages 285–300. Springer.

Lauterbur, P. C. (1973). Image formation by induced local interactions: Examples employing nuclear magnetic resonance. *Nature*, 242:190–191.

Ledberg, A., kerman, S., and Roland, P. E. (1998). Estimation of the probabilities of 3D clusters in functional brain images. *NeuroImage*, 8:113–128.

Liang, Z., MacFall, J. R., and Harrington, D. P. (1994). Parameter estimation and tissue segmentation from multispectral MR images. *IEEE Trans. Med. Imaging*, 13:441–449.

Liu, A. K., Belliveau, J. W., and Dale, A. M. (1998). Spatiotemporal imaging of human brain activity using functional MRI constrained magnetoencephalography data: Monte Carlo simulations. *Proc. Natl. Acad. Sci. U.S.A.*, 95:8945–8950.

Liu, G., Sobering, G., Duyn, J., and Moonen, C. T. (1993). A functional MRI technique combining principles of echo-shifting with a train of observations (PRESTO). *Magn. Reson. Med.*, 30:764–768.

Locascio, J. J., Jennings, P. J., Moore, C. I., and Corkin, S. (1997). Time series analysis in the time domain and resampling methods for studies of functional magnetic resonance brain imaging. *Hum. Brain Mapp.*, 5(3):168–193.

Lötjönen, J., Reissman, P.-J., Mangin, I. E., and Katila, T. (1999). Model extraction from magnetic resonance volume data using deformable pyramid. *Medical Image Analysis*, 3:387–406.

Mansfield, P. (1977). Multi-planar image formation using NMR spin echoes. *J. Phys. C*, 10:L55–L58.

Mansfield, P., Coxon, R., and Hykin, J. (1985). Echo-volumar imaging (EVI) of the brain at 3.0 T: First normal volunteer and functional imaging results. *J. Comput. Assist. Tomogr.*, 19:847–852.

Marchini, J. L. and Ripley, B. D. (2000). A new statistical approach to detecting significant activation in functional MRI. *NeuroImage*, 12:366–380.

McKeown, M. J., Makeig, S., Brown, G. G., Jung, T. P., Kindermann, S. S., Bell, A. J., and Sejnowski, T. J. (1998). Analysis of fMRI data by blind separation into independent spatial components. *Hum. Brain Mapp.*, 6:160–188.

Menon, R. S. (2001). Imaging function in the working brain with fMRI. *Curr. Opin. Neurobiol.*, 11:630–636.

Menon, R. S. (2002). Postacquisition suppression of large-vessel BOLD signals in high-resolution fMRI. *Magn. Reson. Med.*, 47:1–9.

Moonen, C. T. W. and Bandettini, P. A., editors (2000). *Functional MRI*. Springer.

Morris, R. D., Descombes, X., and Zerubia, J. (1996). The Ising/Potts model is not well suited to segmentation tasks. In Lervik, J. M. and Waldemar, P., editors, *Digital Signal Processing Workshop Proceedings*, pages 263–266.

Ngan, S.-C. and Hu, X. (1999). Analysis of functional magnetic resonance imaging data using self-organizing mapping with spatial connectivity. *Magn. Reson. Med.*, 41:939–946.

Nichols, T. E. and Holmes, A. P. (2002). Nonparametric permutation tests for functional neuroimaging: A primer with examples. *Hum. Brain Mapp.*, 15:1–25.

Ogawa, S., Lee, T. M., Kay, A. R., and Tank, D. W. (1990). Brain magnetic resonance imaging with contrast dependent on blood oxygenation. *Proc. Natl. Acad. Sci. U.S.A.*, 87:9868–9872.

Ogawa, S., Menon, R. S., Tank, D. W., Kim, S. G., Merkle, H., Ellermann, J. M., and Ugurbil, K. (1993). Functional brain mapping by blood oxygenation level-dependent contrast magnetic resonance imaging. A comparison of signal characteristics with a biophysical model. *Biophys. J.*, 64:803–812.

Ogawa, S., Tank, D. W., Menon, R. S., Ellerman, J. M., Kim, S. G., Merkle, H., and Ugurbil, K. (1992). Intrinsic signal changes accompanying sensory stimulation: functional brain mapping using MRI. *Proc. Natl. Acad. Sci. U.S.A.*, 89:5951–5955.

Oja, J. M. E., Gillen, J., Kauppinen, R. A., Kraut, M., and van Zijl, P. C. M. (1999a). Venous blood effects in spin-echo fMRI of human brain. *Magn. Reson. Med.*, 42:617–626.

Oja, J. M. E., Gillen, J. S., Kauppinen, R. A., Kraut, M., and van Zijl, P. C. M. (1999b). Determination of oxygen extraction ratios by magnetic resonance imaging. *J. Cereb. Blood Flow Metab.*, 19:1289–1295.

Østergaard, L., Chesler, D., Weisskoff, R. M., Sorensen, A. G., and Rosen, B. R. (1999). Modeling cerebral blood flow and flow heterogeneity from magnetic resonance residue data. *J. Cereb. Blood Flow Metab.*, 19:690–699.

Østergaard, L., Sorensen, A. G., Kwong, K. K., Weisskoff, R. M., Gyldensted, C., and Rosen, B. R. (1996a). High resolution measurement of cerebral blood flow using intravascular tracer bolus passages. Part II:Experimental comparison and preliminary results. *Magn. Reson. Med.*, 36:726–736.

Østergaard, L., Weisskoff, R. M., Chesler, D. A., Gyldensted, C., and Rosen, B. R. (1996b). High resolution measurement of cerebral blood flow using intravascular tracer bolus passages. Part I:Mathematical approach and statistical analysis. *Magn. Reson. Med.*, 36:715–725.

Pappas, T. N. (1992). An adaptive clustering algorithm for image segmentation. *IEEE Trans. Signal Process.*, 40:901–914.

Park, J. and Kurz, L. (1996). Image enhancement using the modified ICM method. *IEEE Trans. Image Process.*, 5:765–771.

Pelizzari, C. A., Ghen, G. T. Y., Spelbring, D. R., Weichselbaum, R. R., and Chen, C. T. (1989). Accurate three-dimensional registration of CT, PET and/or MR images of the brain. *J. Comput. Assist. Tomogr.*, 13:20–26.

Petersson, K. M. (1998). Comments on a Monte Carlo approach to the analysis of functional neuroimaging data. *NeuroImage*, 8:108–112.

Poline, J.-B. and Mazoyer, B. M. (1994). Analysis of individual brain activation maps using hierarchical description and multiscale detection. *IEEE Trans. Med. Imaging*, 13:702–710.

Poline, J.-B., Worsley, K. J., Evans, A. C., and Friston, K. J. (1997). Combining spatial extent and peak intensity to test for activations in functional imaging. *NeuroImage*, 5:83–96.

Pyökkimies, E.-P., Salli, E., and Katila, T. (2001). Fast image order volume rendering algorithm for multimodal image visualization. In *Biomag2000, Proc. 12th Int. Conf. on Biomagnetism*, pages 1043–1045. Helsinki Univ. of Technology, Espoo, Finland.

Rajapakse, J. C., Giedd, J. N., and Rapoport, J. L. (1997). Statistical approach to segmentation of single-channel cerebral MR images. *IEEE Trans. Med. Imaging*, 16:176–186.

Rajapakse, J. C. and Kruggel, F. (1998). Segmentation of MR images with intensity inhomogeneities. *Image Vis. Comput.*, 16:165–180.

Rajapakse, J. C., Kruggel, F., Maisog, J. M., and von Cramon, D. Y. (1998). Modeling hemodynamic response for analysis of functional MRI time-series. *Hum. Brain Mapp.*, 6:283–300.

Rajapakse, J. C. and Piyaratna, J. (2001). Bayesian approach to segmentation of statistical parametric maps. *IEEE Trans. Biomed. Eng.*, 48:1186–1194.

Rosen, B. R., Belliweau, J. W., Aronen, H. J., Kennedy, D., Buchbinder, B. R., Fischman, A., Gruber, M., Glas, J., Weisskoff, R. M., Cohen, M. S., Hochberg, F. H., and Brady, T. J. (1991). Susceptibility contrast imaging of cerebral blood volume: human experience. *Magn. Reson. Med.*, 22:293–299.

Rosen, B. R., Buckner, R. L., and Dale, A. M. (1998). Event-related functional MRI: past, present, and future. *Proc. Natl. Acad. Sci. U.S.A.*, 95:773–780.

Rowe, J. B. and Frackowiak, R. S. (1999). The impact of brain imaging technology on our understanding of motor function and dysfunction. *Curr. Opin. Neurobiol.*, 9:728–734.

Salli, E., Aronen, H. J., Korvenoja, A., Visa, A., and Katila, T. (2001). Effect of analysis strategy on reproducibility of detected fMRI activations. In *Biomag2000, Proc. 12th Int. Conf. on Biomagnetism*, pages 1046–1049. Helsinki Univ. of Technology, Espoo, Finland.

Shahidi, R., Tombropoulos, R., and Grzeszczuk, R. P. (1998). Clinical applications of three-dimensional rendering of medical data sets. *Proc. IEEE*, 86:555–568.

Sipilä, O., Vehkomäki, T., Salli, E., Katila, T., Yu, X., and Ylä-Jääski, J. (1992). General tools for segmentation. In *Proc. of the IEEE EMBS Satellite Symposium on 3D Advanced Image Processing in Medicine*, pages 197–199, Rennes, France.

Skudlarski, P., Constable, R. T., and Gore, J. C. (1999). ROC analysis of statistical methods used in functional MRI: individual subjects. *NeuroImage*, 9:311–329.

Smith, A. M., Lewis, B. K., Ruttimann, U. E., Ye, F. Q., Sinnwell, T. M., Yang, Y., Duyn, J. H., and Frank, J. A. (1999). Investigation of low frequency drift in fMRI signal. *NeuroImage*, 9:526–533.

Talairach, J. and Tournoux, P. (1984). Co-planar stereotaxic atlas of the human brain. *Stuttgart:Thieme*.

Thompson, P. and Toga, A. W. (1996). A surface-based technique for warping three-dimensional images of the brain. *IEEE Trans. Med. Imaging*, 15:402–417.

Thulborn, K. R., Waterton, J. C., Matthews, P. M., and Radda, G. K. (1982). Oxygenation dependence of the transverse relaxation time of water protons in whole blood at high field. *Biochimica et Biophysica Acta*, 714:265–270.

Tiihonen, J., Katila, H., Pekkonen, E., Jääskeläinen, I. P., Huotilainen, M., Aronen, H. J., Ilmoniemi, R. J., Räsänen, P., Virtanen, J., Salli, E., and Karhu, J. (1998). Reversal of cerebral asymmetry in schizophrenia measured with magnetoencephalography. *Schizophr. Res.*, 30:209–219.

Turner, R. and Ordidge, R. J. (2000). Technical challenges of functional magnetic resonance imaging: The biophysics and technology behind a reliable neuroscientific tool for mapping the human brain. *IEEE Eng. Med. Biol. Mag.*, 19:42–54.

Van Leemput, K., Maes, F., Vandermeulen, D., and Suetens, P. (1999). Automated model-based tissue classification of MR images of the brain. *IEEE Trans. Med. Imaging*, 18:897–908.

Villringer, A. and Chance, B. (1997). Non-invasive optical spectroscopy and imaging of human brain function. *Trends Neurosci.*, 20(10):435–442.

Volkow, N. D., Rosen, B., and Farde, L. (1997). Imaging the living human brain: Magnetic resonance imaging and positron emission tomography. *Proc. Natl. Acad. Sci. U.S.A.*, 94:2787–2788.

Williams, D. S., Detre, J. A., Leigh, J. S., and Koretsky, A. P. (1992). Magnetic resonance imaging of perfusion using spin inversion of arterial water. *Proc. Natl. Acad. Sci. U.S.A.*, 89:212–216.

Wolbarst, A. B. (1993). *Physics of radiology*. Prentice Hall International.

Woods, R. P., Cherry, S. R., and Mazziotta, J. C. (1992). Rapid automated algorithm for aligning and reslicing PET images. *J. Comput. Assist. Tomogr.*, 16:620–633.

Woolrich, M. W., Ripley, B. D., Brady, J. M., and Smith, S. M. (2001). Temporal autocorrelation in univariate linear modelling of FMRI data. *NeuroImage*, 14:1370–1386.

Worsley, K. J., Evans, A. C., Marrett, S., and Neelin, P. (1992). A three-dimensional statistical analysis for CBF activation studies in human brain. *J. Cereb. Blood Flow Metab.*, 12:900–918.

Worsley, K. J. and Friston, K. J. (1995). Analysis of fMRI time-series revisited – again. *NeuroImage*, 2:173–181.

Ylä-Jääski, J., Klein, F., and Kübler, O. (1991). Fast direct display of volume data for medical diagnosis. *Comput. Vision, Graphics Image Process.: Graph. Mod. Image Process.*, 53:7–18.

Yu, X., Ylä-Jääski, J., Huttunen, O., Vehkomäki, T., Sipilä, O., and Katila, T. (1992). Image segmentation combining region growing and edge detection. In *Proc. of the 11th IAPR International Conf. on Pattern Recognition*, pages 481–484, The Hague, The Netherlands.

Zarahn, E., Aguirre, G. K., and D'Esposito, M. (1997). Empirical analyses of BOLD fMRI statistics: spatially unsmoothed data collected under null-hypothesis conditions. *NeuroImage*, 5:179–197.

Zhang, Y., Brady, M., and Smith, S. (2001). Segmentation of brain MR images through a hidden Markov random field model and the expectation-maximization algorithm. *IEEE Trans. Med. Imaging*, 20:45–57.